Processing of Aluminum-Nickel Intermetallics by Reactive Infiltration

by

Christopher William San Marchi

B.S., Chemistry (1992)
B.S., Mechanical and Aerospace Engineering (1991)
University of California, Irvine

Submitted to the
Department of Materials Science and Engineering
on January 10, 1997
in Partial Fulfillment of the Requirements for the Degree of

DOCTOR OF PHILOSOPHY IN METALLURGY
AT THE
MASSACHUSETTS INSTITUTE OF TECHNOLOGY

FEBRUARY 1997

Signature of Author: _____
Department of Materials Science and Engineering
January 10, 1997

Certified by: _____
Andreas Mortensen
Professor of Metallurgy

Accepted by: _____
Linn W. Hobbs
John F. Elliott Professor of Materials
Chairman, Department Committee on Graduate Students

Science

Processing of Aluminum-Nickel Intermetallics by Reactive Infiltration

by Christopher William San Marchi

Submitted to the
Department of Materials Science and Engineering
on January 10, 1997
in Partial Fulfillment of the Requirements for the Degree of

DOCTOR OF PHILOSOPHY IN METALLURGY

ABSTRACT

Aligned nickel wire bundles 4-5 cm in length and up to 2.5 cm in diameter were infiltrated by pure aluminum using gas-assisted infiltration. Global compositions in the range 40-76 atomic percent nickel were investigated and found to produce consistent reacted macrostructures after the phase diagram, and independent of applied pressure or volume fraction of the nickel preform. These macrostructures contain a homogeneous NiAl region, with either a Al-rich zone on top, or Ni-rich phases at the sample bottom.

A high-speed digital camera was used to record the infiltration and reaction process in a transparent low-pressure infiltration apparatus. Images showed that infiltration and reaction are independent in time. The gate system directing aluminum flow into the preform caused infiltration to proceed initially in partially-saturated capillarity-driven flow, followed by pressurized "slug flow" infiltration. The average rate of infiltration across the length of the preform was measured using digital images to be 10-100 $cm \cdot s^{-1}$. The infiltrated preform then slowly heated for 2-3 seconds before a combustion front ignited spontaneously at the preform entrance, similar to fronts observed in Self-propagating High-temperature Synthesis (SHS). The combustion front initially featured steady propagation at velocities of 1-10 $cm \cdot s^{-1}$, in agreement with published SHS observations, before becoming unsteady. The several observed macrostructures are explained on the basis of these two separate process steps.

Preforms of nickel pieces (>3 mm diameter) reacted to form macrostructures qualitatively similar to wire preforms. However, nickel powder preforms yielded banded reaction zones of widely different compositions irregularly distributed within the sample. This structure is explained by analysis, assuming rapid reaction concomitant with infiltration.

Thesis Supervisor: Andreas Mortensen
Title: Professor of Metallurgy

Acknowledgments

Some little space and so much thanks... if I could turn this thesis into a page my thanks could fill the rest!

Shall we start with the sponsors? NSF, the sponsors of this project, "cash cow" thank you. I'm appreciative of the Department for providing a teaching assistantship when the coffers were empty. None the less, in the end this document could not have been completed without the generous support of 3M, thank you Tracy and Kamal.

The Andreas Advisor Entity, this document should bear your name, thank you for dragging me (often kicking and screaming) through the hallowed bitter halls of the Institute. I would not have found the checkout stand without your omniscient optimism, ceaseless sedulousness, and, most importantly, your friendship. David Dunand, your inspirations and leadership in the initial murky stages of this study have proved to be insightful and prophetic at the very least, thank you.

I'm thankful to Mert Flemings and his group for the use of their high-speed digital camera and their technical support, without which this study would be much less ambitious. Thank you also to the Edgerton Lab for the use of their high-speed camera which allowed for unprecedented dueling high-speed camera experiments.

Let me express my gratitude to the many undergraduate students that have contributed along the way, especially in the early uncertain stages of this work: Scott, Christian, Andrew, Kevin, and Paul. Christine, you deserve special mention for hacking away the theoretical underbrush in your thesis, I hope it was not too painful. I also want to acknowledge several visiting scientists for their intellectual support, confidence and "helping-hands" in the lab: Anne-Valerie, François, and Christophe.

Of course, I cannot forget the many unfortunate suppliants cast into the MIT tradition along with me: Rob, Pavel, Veronique, Arvind, John, Matthieu, Yusuf, Ali and, especially, Mr. (you'll always be mister to me) Matson for your constant distractions, jargon (buzzz...) and technical expertise. On the other hand—or foot as the case might be—I probably should not resurrect the instigators and accessories—if the shoe fits wear it!—who have kept me... Jimbobob, Spawn, Hackler, Tomala, Keeblerman and

innumerable others. You made it worth every penny I never earned! Please, I must mention Margaret and Gautam, my dearest friends to whom *by the power vested in me by the Commonwealth* I'm bound, and happily so. Also I'm beholden to Gwyneira for her passionate conviction and sanguine praise.

My gracious appreciation to Corinne and Nozomi who gave their valuable time during the preparation of this document *down-the-stretch;* I could not have done it without you, thank you ever-so-much. Naturally, I'm also indebted to all the folks in HQ and around, who have always been extremely helpful if not a source of playful torment.

Finally, this role could not be complete without thanking my family and friends back home who have kept me going with warm thoughts of the Southern Californian sand during these manic New England Winters.

Is that everyone? I can only hope... *hope s'all I gots!*

Me
November 21, 1996
Cambridge, MA

Table of Contents

List of Tables

List of Figures

1. Introduction

Infiltration processes have in recent years demonstrated their utility for the production of composite materials on an industrial scale. In general, these processes have attempted to eliminate reactions between the preform and the melt, although a few investigators have taken advantage of potential reactions between preform and melt to produce novel or refractory materials.

The aluminide systems have received significant attention for many decades as candidates for high-temperature structural applications. Compared with other metallic materials, the processing of aluminides is rendered somewhat more challenging due to their very high melting points. There have therefore been numerous studies on the processing of monolithic NiAl and powder-composite NiAl by reactive techniques. Typically, in such processes, reactions are initiated in packed powder preforms of aluminum, nickel and, in some cases, a reinforcing material such as titanium carbide. However, this technique has proven challenging for the reaction-processing of pore-free materials, and of fiber-reinforced nickel aluminide matrix composites.

Reactive infiltration processing (RIP) is a technique that, like reactive powder processes, utilizes the highly exothermic formation energies of intermetallics, and also, takes advantage of the flexibility of infiltration processing to potentially form complex composite structures, including continuous fiber reinforced intermetallic-matrix composites. This work is an exploration of RIP in the aluminum-nickel system, towards the development of a simple yet effective technique for the production of NiAl and its composites. This system was chosen because it has the following advantages over other aluminide systems: (i) the behavior of the aluminum-nickel system is extensively documented in the literature; (ii) the binary Al-Ni phase diagram is relatively simple compared to other aluminide systems; (iii) NiAl is one of the most exothermic aluminides; (iv) nickel is easy to handle at room-temperature and elevated temperatures; and (v) nickel is relatively economical.

Specifically, this thesis focuses on the production of samples based on the NiAl intermetallic phase, free of microstructural defects such as pores, and with controlled macrosegregation. It begins with a brief review of the relevant

combustion synthesis literature, foundations for infiltration studies, and a summary of the few investigations of RIP in which the engineering potential for this process is evident, at least for the aluminide family of materials. After developing the terminology and an appreciation for previous work, a description of the important thermodynamics in combustion synthesis is presented, with emphasis on the Al-Ni system.

The experimental apparatus used to produce NiAl by RIP and the analytical tools used to study the process are described in Chapter Four. The results of the study are presented in Chapter Five, followed by their discussion. Reactions by their very nature are system-specific; however, for generality, results are discussed by considering two limiting cases: (i) very rapid reaction in relation to infiltration; and (ii) very slow reaction in relation to infiltration. As will be shown, results from this work focus on the latter limit, because it yields attractive macrostructures. For this reason most of the work was conducted using aligned nickel wire preforms for the production of NiAl. The discussion is followed by a few summarizing remarks and suggestions for future work.

2. Literature Survey: Combustion Synthesis of Nickel Aluminides

2.1. Combustion synthesis

Combustion synthesis or reactive synthesis describes a broad range of techniques for processing materials by means of highly exothermic reactions on time scales ranging from seconds to minutes. The thermite reaction, which was explored at the beginning of the twentieth century for metal-oxide mixtures, provides perhaps one of the oldest examples [1]. In the 1960s, self-propagating combustion synthesis of ceramic systems, including many of the carbides, borides and silicides, was intensively researched in the former Soviet Union as an outgrowth of solid-state combustion studies. In recent years, this method of materials synthesis has been actively explored in many countries, notably the United States, for the synthesis of advanced refractory materials.

Thus, combustion synthesis methods have been investigated as an alternate processing technique for the formation of intermetallic compounds with high melting points. Although the heat released upon formation of an intermetallic compound from its elements is typically lower than for ceramics, it has been shown that a number of intermetallics, including the aluminides of titanium and nickel, release enough heat to produce self-sustaining reactions in combustion synthesis.

Combustion techniques have several advantages over conventional non-reactive processes such as melting and casting, or non-reactive powder metallurgy [2]: (i) simplicity and speed; (ii) low energy requirement for the process itself, since there is significant energy released by the reaction, such that some systems can be ignited with a torch at room temperature; (iii) high purity of the resulting material compared to conventional powder metallurgy or ingot processes: the extreme temperatures in the combustion front remove volatile contaminants, and prolonged contact with potential contamination sources such as crucible walls is avoided; (iv) production of complex and metastable phases: thermodynamically unstable phases or two-phase materials can be produced *in situ*, such as a TiC reinforced NiAl from elemental powders [3]; and (v) relatively simple tooling requirements.

General disadvantages intrinsic to condensed phase combustion synthesis include the following [2]: (i) phase homogeneity can be difficult to achieve in multi-phase systems; (ii) thermal gradients, on the order of 10^5 K/cm, develop large residual stresses and can cause cracking in the product material; (iii) the combustion reactions are difficult to control; (iv) near-net shape processing from powders can be challenging due to volume changes and melting; and (v) the resultant materials are nearly always highly porous due to the initial porosity of the reactant preforms, evolution of gases during combustion, volume changes upon phase formation, and solidification shrinkage. In spite of these disadvantages, combustion synthesis has been used in the former Soviet Union to produce molybdenum disilicide heating coils and powder materials on an industrial scale [4].

Two basic modes of powder-based combustion synthesis have been distinguished in the literature [5]. The first is termed the "thermal explosion" mode, and is characterized by the fact that the entire sample is heated simultaneously, usually by placing it in a furnace. The other is termed the wave front combustion mode, generally referred to as Self-propagating High-temperature Synthesis or SHS: here the sample is heated locally by a flame or electrical discharge, to initiate a self-sustaining combustion/reaction front that propagates through the sample, forming the product in its wake. The distinction between these two modes is in fact based solely on practical processing considerations, since "explosion combusted" samples may actually have been dominated by wave-front phenomenon. This was, in particular, shown to be the case for the aluminum-nickel system: combustion fronts were observed in Al-Ni powder samples processed nominally in the "thermal explosion" mode, by heating in a furnace [6, 7].

Due to the very high processing temperatures realized in reactive synthesis and the highly transient nature of the combustion process, often little is known about the thermal kinetic properties and phase transformations (or structural macrokinetics) during combustion. Many studies rely on empirical observations and highly simplified assumptions when attempting to untangle the complex series of events leading to the final material. Moreover, reactive synthesis is highly dependent on temperatures, preform activity, and material system. As a result, many seemingly contradictory reports have been made, for example with respect to the influence of powder size on the combustion processes. This underscores both

the flexibility of the process, and the need to carefully consider all of its facets, from the production of the preform material and the purity of the melt, to the fluid flow characteristics and the reaction kinetics.

Combustion methods for the formation of Al-Ni intermetallics, defined by the phase diagram in Fig. 2.1, utilize many forms of precursor materials. The most common method makes use of mixed elemental powders (*e.g.*, aluminum and nickel) that are compacted into preforms and reacted to form the product phase (*e.g.*, NiAl or Ni_3Al), although some work has also been done with foils [8, 9, 10, 11] and multi-layer films [12, 13, 14]. Of these, only powder-based preforms provide versatility in final part shape and dimensions; hence powder methods for the production of Al-Ni intermetallics are the focus of the following brief survey.

2.2. Combustion synthesis in the Al-Ni system by global heating: "thermal explosion" mode

Reactive sintering, reactive hot isostatic pressing, and reactive hot pressing have all been used for the production of intermetallics and intermetallic composites based on the aluminum-nickel system [5, 6, 11, 15, 16, 17]. Reactive sintering simply consists in heating a compact of elemental powders to temperatures at which reactions are initiated between the precursor powders to form the product, whereas reactive hot isostatic pressing and reactive hot pressing make use of pressure, provided by a HIP unit or applied uniaxially, to densify the product phase during reactive sintering. German *et al.* have produced Ni_3Al by heating elemental powder compacts to ~600°C, near the aluminum-rich eutectic temperature, 640°C, Fig. 2.1 [16]. Solid-state reactions during the initial stages of reactive sintering heat the compact and form a continuous transient liquid phase that spreads rapidly, densifying the structure provided that the aluminum powder size is (i) smaller than the nickel powder size such that large pores are not left behind by the melting aluminum, yet (ii) large enough so that oxide does not influence the kinetics or prevent spreading of the liquid Al. The heating rate is an important parameter in controlling the reactions: low heating rates allow significant solid-state reactions to occur prior to formation of the liquid, which lowers the quantity of liquid formed; high heating rates on the other hand make process control difficult [5, 16].

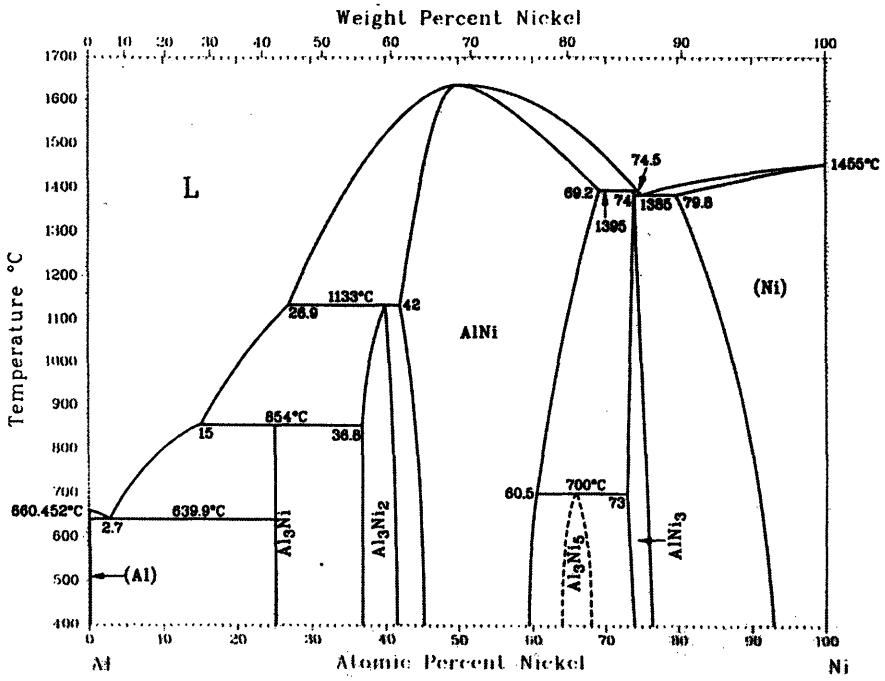

Fig. 2.1. Binary Al-Ni phase diagram from Ref. [18].

Several investigators have reported that self-sustaining reactions do not develop everywhere simultaneously during reactive sintering of Ni_3Al; rather, combustion fronts develop and propagate through the sample. Nishimura and Liu have measured velocities of 6 $cm \cdot s^{-1}$ in reactively sintered samples and have also observed that heat loss via conduction can result in the formation of lower melting intermetallics, namely Al_3Ni_2, in the final product [6].

NiAl formation is more difficult to control because the heat evolved is significantly larger and causes melting of the product. Several studies have shown that NiAl powder can be added to the compact as a heat sink to lower the adiabatic reaction temperature, so that free-standing preforms do not slump due to melting of the product NiAl [15].

Investigators have successfully produced many Al-Ni-based composite materials by reactive sintering and these are reviewed in Ref. [19].

2.3. Combustion synthesis by localized heating: Self-propagating High-temperature Synthesis (SHS)

2.3.1. Theory: front propagation velocity and stability

The structure, velocity, and stability of a propagating reaction front in condensed phases have been the subject of a relatively vast body of research, summarized in several recent reviews [2, 4, 20, 21]. Analysis of the SHS problem relies on a global or *macroscopic* description of the process and a local or *microscopic* description of the dependence of local reaction kinetics on the temperature, fraction material transformed, and initial reactant structure. The macroscopic approach uses mass and thermal transport to model the process on a length-scale similar to that of the entire sample.

Microscopic kinetic studies have used two formulations: the "homogeneous reaction" formulation, which assumes conventional Arrhenius finite-order kinetic expressions, and the "heterogeneous reaction" formulation, which assumes mass transport by diffusion, generally across a reaction product layer. The latter formulation is either proposed in a general form (given below), or incorporated in an overall combustion model by authors who propose a defined self-coherent physical model of the process, which includes an assumed given microscopic configuration for the reactant mixture (*e.g.*, alternating layers of each element aligned parallel or perpendicular to the propagating front).

Experimental evidence has shown that the front propagation rate in the Al-Ni system depends on initial powder or foil size and morphology [13, 22, 23, 24]. From this observation it seems reasonable to assume that diffusion intervenes in the local reaction kinetics and that heterogeneous diffusion-based formulations are the most appropriate for the Al-Ni system. Thus, for heterogeneous reaction kinetics, the stable propagation velocity of a combustion front is given by the general form:

$$u^2 = B \frac{\alpha T_c^2}{E(T_c - T_o)} \exp\left(\frac{-E}{RT_c}\right) \qquad (2.1)$$

where T_c is the combustion temperature, T_o the initial reactant temperature, α

is the thermal diffusivity of the unreacted material ahead of the reaction zone, R is the universal gas constant, and E is the activation energy from the local reaction law [21].

Heterogeneous local kinetic laws typically have the general form:

$$\phi = A \exp(- m \eta) \eta^{-n} \exp(-E/RT) \tag{2.2}$$

where ϕ is the rate of reaction, η is fraction converted reactant, and m and n are constant exponents. For reactions limited by diffusion through a planar reaction layer, m = 0, and n = 1. In the equations above, A and B are constants, typically inversely proportional to the square of the microstructural period distance for the initial reactant. This is shown, for example, in the more specific expression derived by Armstrong and Koszykowski [25] for the propagation velocity of a front caused by single-phase exothermic mixing of two, initially segregated, layers of pure elements. This expression particularly applies when the reaction takes place by diffusive intermixing of two liquid phases, as is the case, in principle, in the present experiments, for which the adiabatic temperature typically exceeds the melting point of both reactants. When derived according to the regular solution model, the model of Armstrong and Koszykowski yields:

$$u^2 = 6A \frac{RT_c}{E} \left(\frac{\alpha}{\delta}\right)^2 \frac{T_c}{(T_c - T_o)} \exp\left(\frac{-E}{RT_c}\right) \tag{2.3}$$

where A and E are defined such that:

$$Le^{-1} = \left(\frac{D}{\alpha}\right) = A \exp\left(\frac{-E}{RT}\right) \tag{2.4}$$

where D is the interdiffusion coefficient of the binary liquid phase, and Le is the Lewis number. E is approximately the activation energy for diffusion, because α has only a moderate dependence on temperature at elevated temperatures; hence this expression is of the same form as eqn. (2.1). The half-period distance across the assumed lamellar aluminum-nickel initial microstructure, δ, now appears explicitly in the velocity expression. Moreover, in eqns. (2.1) and (2.3), the combustion temperature T_c is equal to the thermodynamically derived adiabatic temperature T_{ad} if the reaction goes

to completion, η =1, in the reaction zone, that is, if there is no "after-burning" behind the front.

Combustion waves can, however, become unstable, both in time and in morphology: unsteady fronts of many forms have been identified, including the oscillatory and spin combustion modes [4]. In experimental practice, unstable front propagation is identified either by observation of the specimen surface during combustion, or by metallographic analysis of the resulting microstructure: unstable fronts tend to produce layered, or otherwise segregated, macrostructures [23, 24].

Margolis analyzed the stability of a steady-state propagating front with heterogeneous local reaction kinetics, typical of a reaction controlled by diffusion through a growing interlayer [21, 26]. Neglecting the separation of nickel melting and reaction front propagation, and assuming heterogeneous front kinetics as above with m = 0 and n = 1, the expression of Margolis reduces to the simple criterion:

$$\frac{E\,(T_c - T_o)}{RT_c^2} < 8 \qquad (2.5)$$

for front stability against all perturbation wavelengths. An alternate criterion by Zeldovich

$$\frac{E}{RT_c} \leq 9.1\,\frac{Cp\,T_c}{\Delta H} - 2.5 \qquad (2.6)$$

for front stability, where ΔH is the total heat of the reaction and Cp the heat capacity of the reaction product, is cited in the review by Munir and Anselmi-Tamburini [2] and by Naiborodenko and Itin [27].

2.3.2. Kinetics of reaction propagation: SHS of NiAl

The Al-Ni system has been the subject of several quantitative kinetic studies in self-propagating combustion synthesis, including a series of papers by Naiborodenko and Itin [22, 27, 28, 29], and Maslov *et al.* [30] in the former Soviet Union during the 1970s. Other, more recent, data on front velocity and stability can be found in Refs. [13, 14, 23, 31]; these explore the influence of

reactant particle or layer size, but, unlike the Soviet studies, do not investigate the role of the initial temperature T_o or of the diluent concentration.

Assuming the linear form of eqn. (2.1)

$$\ln\left(\frac{u}{T_c}\right) = a - \frac{E}{2R}\left(\frac{1}{T_c}\right) \tag{2.7}$$

where a is approximately constant, it was shown in Ref. [27], where T_c was confirmed by experimental measurement, that the activation energy E is, in fact, constant for equiatomic Al-Ni mixtures, *i.e.*, straight lines were obtained in a plot of $\log(u/T_c)$ versus $1/T_c$. This confirms theoretical equations for velocity as a function of initial temperature T_o and diluent volume fraction if $(T_c - T_o)$ varies relatively little as these two parameters are varied. This is generally true if T_o alone is varied, but somewhat less so if, as in the work of Naiborodenko and Itin, T_c is varied by varying the concentration of diluent NiAl. Analysis shows that the velocity increases as the reactant powder size decreases, an observation subsequently confirmed for equiatomic Al-Ni powder mixtures [23] and multi-layer samples [13, 14]. For the fine-grained powder samples of Naiborodenko and Itin, plots of $\log(u/T_c)$ versus $1/T_c$ exhibited a decrease in slope as T_c exceeded the melting point of nickel [27]. This change in slope was taken to indicate a change in rate-controlling mechanism as nickel melts, the rate controlling mechanism being liquid-state diffusion when nickel is molten, with E = 60 $kJ \cdot mol^{-1}$, compared with a much higher value of E = 140 $kJ \cdot mol^{-1}$ at T_c lower than the melting point of nickel (corresponding to higher dilution). Data for large nickel particles (41-73 μm) have shown a constant value of E = 140 $kJ \cdot mol^{-1}$ independent of T_c relative to the melting point of nickel.

Data of Maslov *et al.* [30] for NiAl were obtained by varying both the diluent concentration and the initial reactant temperature T_o using a single powder type (the nickel particle size was below 45 μm, the aluminum powder was much smaller, 1-5 μm). These show that front propagation velocity is a direct function of T_c, except when T_c equals the NiAl congruent melting temperature, at which value u varies between a low value for production of fully solid NiAl, and a higher value for production of fully liquid NiAl. In fact, the data of Maslov for front velocity vary continuously with either diluent concentration or initial temperature T_o, such that the front velocity u

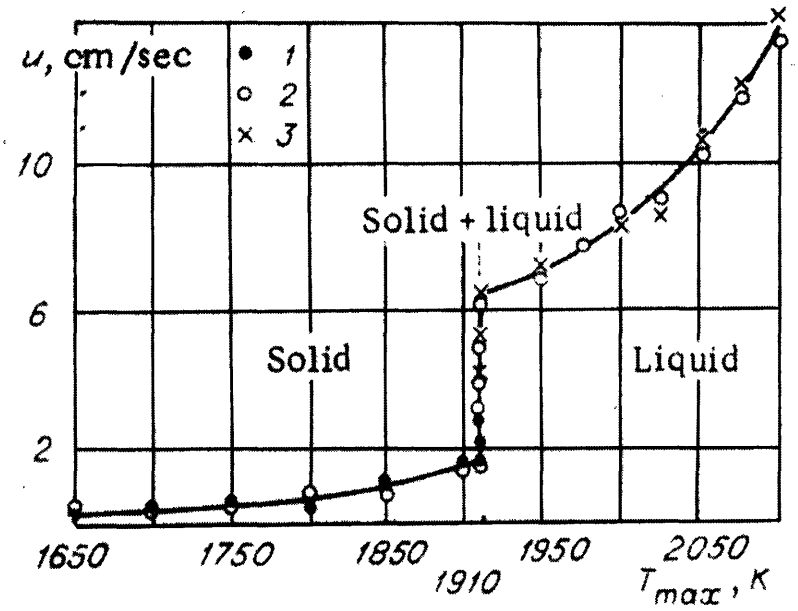

Fig. 2.2. Data of Maslov *et al.*, combustion front velocity u versus combustion temperature T_c from Ref. [30].

seems rather to be a well-defined function of final product enthalpy, and not temperature T_c.

The data of Maslov for the formation of NiAl by combustion synthesis are shown in Fig. 2.2. Plotting the data using eqn. (2.7), it can be shown that the data correspond to an activation energy of 235 kJ·mol^{-1}. This value is significantly higher than the values obtained by Naiborodenko *et al.* It is, thus, possible that oxide layers covering the very small aluminum powders intervened in the local reaction mechanisms.

Unsteady propagation has been observed in the NiAl system, and its onset attributed to thermal transport and to kinetic factors. An increased rate of heat conduction away from the reaction front has been proposed as a cause for front instability, because it has been observed that as the initial powder packing density is increased, front propagation tends to become unstable [22]. Alternatively, the formation of solid intermediate phases has been proposed to act as diffusion barriers which causes unsteady wave propagation [5].

The front stability criterion in eqn. (2.6) was tested against experimental data by Naiborodenko and Itin on the combustion synthesis of equiatomic NiAl, and good agreement was found [27]. It is interesting to note, also, that

transitions observed by Li and Sekhar [23], who found that front stability was lost as the reactant particle size was increased, and by Naiborodenko and Itin, who found that front stability was lost as preform porosity increased, are not predicted by theoretical expressions in eqns. (2.5) and (2.6), since neither preform thermal conductivity nor particle size enter these equations.

2.3.3. Combustion wave structure: SHS of NiAl

As a complement to studies of reaction-front propagation, sophisticated techniques have been developed to probe the combustion wave structure in SHS processes. Fig. 2.3 illustrates schematically the temperature profile, extent of reaction, and rate of reaction within the classical "equilibrium" combustion wave and the non-equilibrium combustion wave [4]. In equilibrium wave structure, all chemical and phase transformations occur in a narrow region at the combustion front. These conditions are generally realized when solid products are formed in the combustion wave, or in systems with low propagation velocities. Rapid SHS processes are believed to proceed with a different "non-equilibrium" wave structure; metastable phases are formed at the front, with the final phase transformation only occurring significantly behind the combustion front.

Aleksandrov *et al.* have suggested that many SHS systems are characterized by non-equilibrium combustion front propagation, and proposed a precipitation mechanism to explain intermediate stages of reaction in general [32, 33]. By observation of Al-Ni samples interacting under a transmission electron microscope, Aleksandrov *et al.* proposed that the specific reaction mechanism between the Ni and Al phases is one of concomitant diffusion of aluminum into the solid nickel and dissolution of nickel into the aluminum melt through an intermediate solid layer of roughly constant width that separates the solid nickel from the melt, and moves rapidly towards the center of Ni particles. NiAl is then believed to precipitate independently within the supersaturated melt [33].

This type of transient transformation mechanism was observed in the first X-ray phase analysis by synchrotron radiation diffractometry of combusting equiatomic Ni-Al samples. Boldyrev *et al.* showed that NiAl does not form at the reaction front, but appears only 70 s after passage of the front, and that its formation is preceded by the formation of two unknown intermediate phases

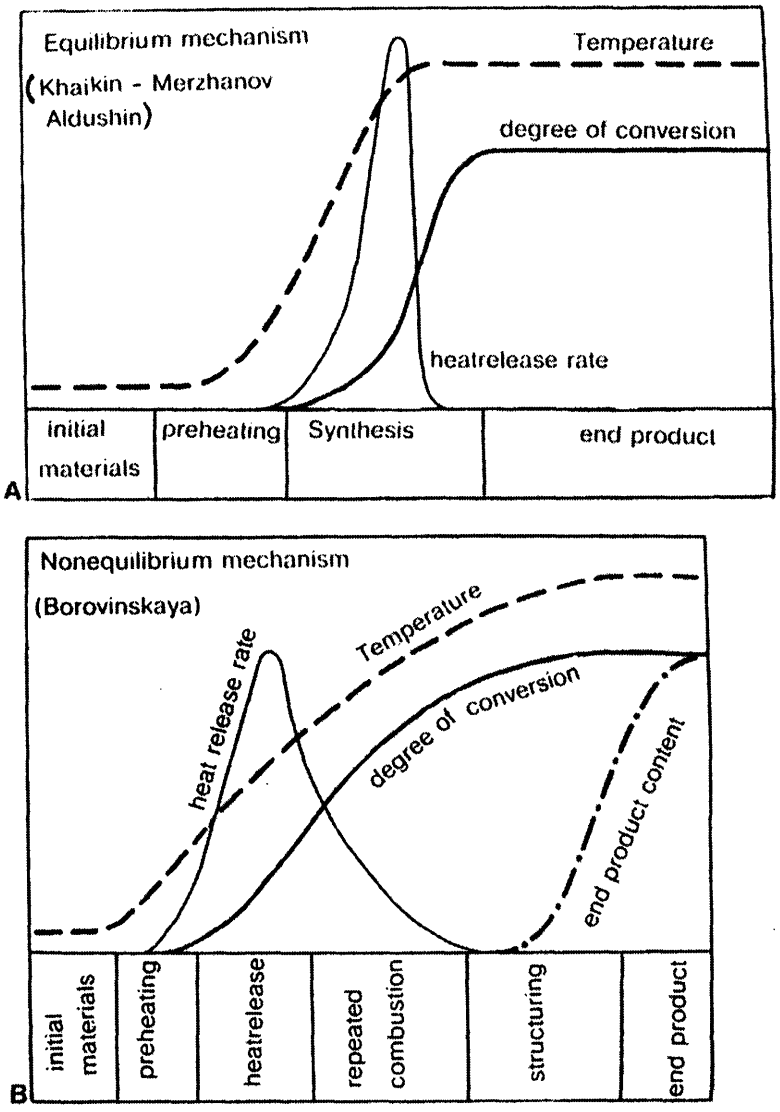

Fig. 2.3. Structure of combustion front from Ref. [4]: (A) equilibrium mechanism, and (B) non-equilibrium mechanism.

[32, 33, 34]. This x-ray technique has since been called time-resolved x-ray diffraction (TRXRD) and investigators in the US have made similar studies increasing the temporal resolution to 10 ms [35, 36]. Synchrotron techniques have also been extended to include a technique for monitoring the local atomic coordination of nickel, called the quick scanning extended x-ray absorption fine structure (QEXAFS) technique [37].

Another Russian group has more recently (1994) performed TRXRD studies, noting the importance of careful and proper treatment of the data to

obtain meaningful information [38]. For example, they note that observations in different regions of the spectra can provide conflicting evidence, thus statistical considerations are necessary to characterize the complex events in these multi-phase systems. Nevertheless, all the above studies concur in observing qualitatively similar phenomena: formation of intermediates prior to the formation of the end-product, which only forms significantly after the passage of the reaction front.

Volpe *et al.* obtained results from a high-speed one-color pyrometry technique that seemingly contradict the above studies [39]. Yet, while they recognize the importance of dissolution, they assume *a priori* an equilibrium structure and consider, it seems, only the first one hundred milliseconds of interaction. Furthermore, the importance of experimental parameters (powder sizes, powder production methods, temperatures, etc.) is well understood, yet, surprisingly, this study and many of the studies above do not report the experimental parameters used, making it difficult, if not impossible, to develop a complete coherent understanding of the broad findings in the literature.

2.4. Reactive infiltration processing (RIP) of intermetallics

2.4.1. Definition and general features of reactive infiltration

Infiltration is the process by which a molten material is forced into a porous preform, which may be at a different temperature than the melt. Gravity or capillary forces can be used in wetting systems as the driving force for infiltration, such as the infiltration of carbon with silicon alloys [40]. Similarly, reactive metal penetration of dense ceramics utilizes reactive wetting phenomena in the production of metal-matrix composites [41, 42]. Non-wetting systems, such as aluminum-alumina require pressure to drive the metal into the preform. Pressure-assisted infiltration of non-reacting fibrous and particulate preforms has been used commercially to produce reinforced aluminum-, magnesium-, zinc-, and copper-based alloy matrices, and has been extensively documented both theoretically and experimentally [43]. Infiltration processing techniques have several important advantages over traditional foundry methods [44]: (i) near-net shape processing of materials that have little or no machinability; (ii) conservation of preform

integrity (assuming a non-reacting system); and (iii) efficiency, both saving time and lowering material costs.

Reactive infiltration processing (RIP) is a technique whereby a melt infiltrates a porous perform with subsequent or concomitant reactions between the solid preform and the liquid infiltrate. RIP of aluminides has several advantages over combustion synthesis while incorporating the advantages of both infiltration processing and combustion synthesis: (i) the use of liquid aluminum eliminates the oxide layer on individual aluminum powders; (ii) porosity, inherent to powder metallurgical techniques, is reduced or eliminated by the forced infiltration of a liquid; (iii) the integrity of fibrous or whisker reinforcements is conserved compared to powder metallurgical techniques; (iv) near-net shape processing is possible, slumping of compacts during SHS processing being of no concern because the preform is contained in a mold or crucible; and (v) speed.

2.4.2. Analysis of reactive infiltration

Infiltration processes in general are governed by Darcy's law, which states that

$$v_o = \frac{-K}{\mu} \left(\nabla P - \rho_m g \right) \tag{2.8}$$

where v_o is the superficial velocity, K is the symmetric permeability tensor of the preform, μ is the viscosity of the liquid metal, P is the average pressure, ρ_m is the density of the infiltrate, and g is the acceleration due to gravity. Neglecting the effect of gravity and invoking continuity, the average velocity v is

$$v = \frac{- K \nabla P}{\mu (1-V_p)} \tag{2.9}$$

where V_p is the volume fraction of the preform. Many correlations exist for the prediction of K from the morphology of the preform, the simplest and most widely used being the Blake-Kozeny equation:

$$K = \frac{(1-V_p)^3}{4.2\ S_o^2\ V_p^2} \tag{2.10}$$

where S_o, the specific surface area, is the total surface area of the preform per unit preform volume; for example, the specific area for a packed bed of perfect spheres with uniform radius r_s is simply $S_o = 3/r_s$. In general, K is a complicated function of time and position, particularly in reactive systems where the pores change size (and shape) as reactions proceed.

The pressure P is the sum of the applied pressure and the capillary pressure inherent to the system. Capillary forces at regions of coexistence of infiltrate, preform and gas phases influence infiltration kinetics significantly, and in pressureless infiltration these forces drive the entire process. In non-reactive wetting, capillary forces are characterized using the contact angle of the infiltrate on the preform solid. A simplified description of wetting, known as the slug-flow assumption, is useful in calculating the overall infiltration kinetics; however, in some cases, it can provide an oversimplified description of the complex microscopic phenomena that occur during infiltration.

Wetting phenomena have been studied extensively in hydrology with the use of drainage/imbibition curves [45, 46] which show the dependence of saturation, or the degree of wetting in the porous solid, on the pressure difference between the wetting phase and a non-wetting phase, *i.e.*, the capillary pressure. Drainage/imbibition curves show that there is not a direct functional relationship between saturation and pressure, rather there is a significant amount of hysteresis in the drainage and imbibition processes, and any point on the series of curves can be reached by an infinite number of pressure change paths. This irreversibility occurs because energy is mechanically lost in the process of drainage and imbibition of the porous medium, even if there are no chemical reactions between the preform and infiltrate, due to constrictions in pore geometry ("Haines jumps"), and roughness or lack of chemical homogeneity on the preform surface. In addition, an irreducible saturation, usually expressed as the volume fraction of pore space occupied V^{ir}, is observed, below which the preform cannot be "dewetted" [45]. This condition is reached when the wetting fluid is reduced to a volume fraction such that it can no longer form a continuous fluid phase within the preform and "islands" of the wetting phase become isolated. This

phenomenon, of course, is complicated by chemical interactions between the liquid and solid phases.

Theoretical analysis specifically relevant to condensed phase reactive infiltration is relatively scarce in the literature, despite tangible engineering importance of the process (*e.g.*, in the production of Si-SiC composites). One reason for this is that process kinetics are very system-specific. In particular, relative magnitudes of chemical interaction and fluid flow can vary widely, as can the possible nature of chemical reactions and phase equilibria involved.

In RIP systems of highly reactive systems with low permeability and hence low infiltration rates, reaction choking can be a problem: this has been observed in both capillary infiltration [40] and pressure-assisted infiltration [47]. Reaction choking occurs when solid products form in the pores of the preform during infiltration, essentially filling the pores and stopping or "choking" the infiltration. Messner and Chiang [48] developed a model for reactive choking for the infiltration of silicon carbide with silicon-molybdenum alloys.

Macrosegration is also a significant problem in systems that react intensely during infiltration, particularly in systems where the preform has significant solubility in the infiltrating material. Indeed, solid reactant dissolution can result in large concentration gradients as the solute is transported with the infiltration front [49].

At the opposite extreme, when there is a relatively low rate of reaction compared to the rate of infiltration, the liquid essentially permeates the preform before any reaction proceeds. In this case, the infiltration and the reaction processes are decoupled to the extent that infiltration kinetics can essentially be predicted without taking macroscopic reaction into account.

2.4.3. Reactive infiltration processing of intermetallics and their composites

Squeeze casting techniques have been used to produce intermetallics [50], intermetallic based composites [47] and distributed intermetallic aluminum matrix composite materials [51, 52]. Processing techniques, and to some extent the microstructures that were desired, varied significantly from study to study.

Suganuma [50] produced monolithic nickel aluminides, based on Ni_3Al, by sintering 44 μm nickel powder to various densities, and then infiltrating

with aluminum using a squeeze casting press. The text of this article implies full infiltration and full reaction of 3.5 cm diameter by 0.8 cm high cylindrical preforms. The tensile strength of the resulting monolithic samples was measured to be "about 400 MPa."

Fukunaga *et al.* [47] also used squeeze casting in an attempt to produce titanium aluminide composites *in situ* by infiltrating titanium oxide preforms with aluminum, according to the reaction:

$$3\ TiO_2 + (7+x)\ Al \rightarrow 3\ TiAl + 2\ Al_2O_3 + x\ Al \qquad (2.11)$$

Fukunaga theorized that reaction would occur concomitant with infiltration, resulting in the formation of a solid reaction layer that narrows the pore channels, eventually restricting the flow of the molten aluminum, *i.e.*, reaction choking, as observed and modeled for capillary driven reactive infiltration of carbon by silicon [48]. Although Fukunaga gives no details about his TiO_2 whisker preforms other than size (4.8 cm diameter by 1.5 cm height), one can assume that whiskers are fine, and hence that the permeability is small ($<10^{-8}$ cm^2). This process, as conducted, should therefore indeed be highly sensitive to reaction choking. Fukunaga also observed significant preform compression in his experiments.

Colin *et al.* have been using a squeeze casting technique in an attempt to produce stainless steel fiber reinforced aluminum matrix composites. However, they have found that the complex interaction between solidification and reaction causes significant problems in achieving unreacted but fully infiltrated samples on one hand, and fully infiltrated and completely reacted on the other [53, 54, 55].

Gas-pressure infiltration techniques have also been used by several investigators to produce nickel aluminides and composites. H. Chen *et al.* produced nickel aluminide matrix composites by submersing preforms in a bath of aluminum followed by pressurization of the surface of the fluid with gas to drive the infiltration [49]. The preforms contained nickel powder of two types (5-7 μm and 44-150 μm diameter powder) and either Al_2O_3 fibers or TiB_2 particles packed to an overall density of >60%. H. Chen *et al.* give no quantitative dimensions of the samples, but they identify several reaction zones which are attributed to dissolution of the preform during infiltration and transport of nickel with the infiltration front, resulting in regions

depleted in nickel ($NiAl_3$), and regions rich in nickel (Ni_3Al), in addition to a NiAl region.

A tensile strength of 425 MPa was measured by Y. Chen and Chung [56] for Ni_3Al by RIP. In this study, fine nickel particles (3-7 μm) sintered to form preforms 78% nickel by volume were infiltrated with pure aluminum using gas pressure. Wet-formed preforms were 58% nickel by volume and produced an aluminum-matrix $NiAl_3$ composite when infiltrated under the same conditions as the denser preforms.

Dunand *et al.* used several techniques, including a gas pressure technique, to produce NiAl and NiAl reinforced with alumina particles [57, 58]. Preforms produced in this work, which measured 0.7 cm in diameter by 3 cm in length, were prepared using nickel powders in two size ranges: 5-15 μm or 150-220 μm. Dunand *et al.* also controlled the preform temperature independently of the molten aluminum temperature in some experiments, as a method of controlling the reactions. In these experiments, smaller preforms, 1.2 cm in diameter and 1.2 cm high were used. A variety of microstructures were found, ranging from barely reacted nickel surrounded with alloyed aluminum to fully reacted, dendritic NiAl. Additional microstructures comprising zones of varying composition, including a region seemingly containing unreacted nickel particles surrounded by a nickel-rich phase and macroscopic aluminum-rich veins, were formed. Overall, results from this study showed that, depending on processing parameters, a wide variety of structures could be obtained, featuring widely varying degrees of interaction and frequent extensive macrosegregation.

The samples of fully reacted, relatively homogeneous and essentially dense Ni_3Al and NiAl produced in the work of Suganuma [50] and of Dunand *et al.* [57, 58] respectively, illustrate the utility of RIP for the production of aluminides. Similarly, the production of long fiber composites by H. Chen *et al.* [49] demonstrates the potential of RIP as a method of producing a new class of materials, namely continuous fiber reinforced high-temperature structural intermetallics, for which powder metallurgical techniques are generally inadequate. Furthermore, novel and complex microstructures are easier to control during rapid reactive synthesis; an example of such microstructures is provided by the lamellar $NiAl/Ni_3Al$ structure observed by H. Chen *et al.*, which the authors suggest may provide a method of ductilizing NiAl-matrix materials. These studies demonstrate the

engineering potential of reactive infiltration processing in the Al-Ni system, and also, the wide array of structures that can be generated. However, these investigations lack an understanding of the physical phenomena inherent to the process; therefore, the aim of the present study is to further develop a basic understanding of the governing principles of RIP, so as to provide the first step towards the production of advanced refractory structural materials having controlled and potentially unique structures by the method.

3. Thermodynamics

3.1. Enthalpy of solid phases

While relatively complete thermodynamic data are available for solid phases in the Al-Ni system, there are often inconsistencies. For example, values for the enthalpy of formation for NiAl have been reported in the literature varying from 58.8 to 72 $kJ \cdot mol^{-1}$ [59]. Therefore, for consistency, it was deemed best to use the data of Kubaschewski *et al.* [60], since this reference provides a complete and self-consistent set of temperature-dependent thermodynamic data for the pure elemental phases, and for each intermetallic in the Al-Ni system.

In this reference, a single functional form is used for the heat capacity, Cp, as a function of temperature [60]:

$$Cp(T) = A + BT + \frac{C}{T^2} + DT^2 \tag{3.1}$$

where A, B, C, and D are constants, and T is the temperature in Kelvin. The enthalpy of formationof a given phase at a temperature T^* from the elements in their standard state at 298K, $\Delta H(T^*)$, is

$$\Delta H(T^*) = \Delta H(298K) + \int_{298K}^{T^*} Cp(T)\, dT \tag{3.2}$$

where Cp(T) is the heat capacity of the phase in question, assumed not to change state between 298 K and T^*. Substituting Kubaschewski's form for Cp, eqn (3.1), into eqn. (3.2) and integrating, the temperature-dependent enthalpy of each phase then takes the form:

$$\Delta H(T) = AT + \frac{B}{2}T^2 - \frac{C}{T} + \frac{D}{3}T^3 + E \tag{3.3}$$

where E is a constant. Values of the five constants A, B, C, D and E from eqn. (3.3) are presented in Table 3.1 for each phase in the Al-Ni system. Note that, for the functions from Table 3.1, the standard states are pure nickel and

Table 3.1. Constants giving the temperature-dependent enthalpy in $J \cdot mol^{-1}$ for the phases in the Al-Ni system according to eqn. (3.3), from data in Ref. [60].

phase	temperature range (K)	A	B x 10^3	C x 10^{-5}	D x 10^6	E x 10^{-3}
Al (s)	298 - 934	31.38	-16.40	-3.60	20.75	-100.1
Al (l)	≥ 934	31.76	0.0	0.0	0.0	-0.801
Al_3Ni	298-1127	84.10	35.15	0.0	0.0	---
Al_3Ni_2	298 - 1406	106.06	34.31	0.0	0.0	-315.5
NiAl (s)	298 - 1912	41.84	13.81	0.0	0.0	-131.5
NiAl (l)	≥ 1912	71.13	0.0	0.0	0.0	-99.44
Ni_3Al	298 - 1668	88.49	32.22	0.0	0.0	-180.9
Ni (s)	298-631	11.17	37.78	3.18	0.0	-3.94
	631-1728	20.54	10.08	15.40	0.0	-2.40
Ni (l)	≥ 1728	38.91	0.0	0.0	0.0	-2.79

aluminum at 298K and all subsequent reference to enthalpies assumes this standard state, unless otherwise noted.

The enthalpy of formation for each phase $\Delta H(T^*)$ varies according to composition and temperature. For all phases other than NiAl, however, its variations with composition are negligible, compared to the error associated with the data, because the compositional width of relevant phase fields is narrow. NiAl, on the other hand, has a relatively broad phase field on the phase diagram, Fig. 2.1. For this phase, therefore, the actual enthalpy of off-stoichiometric compositions is calculated by assuming that the intermetallic is made of stoichiometric NiAl, and excess atoms having the enthalpy of the pure element in the solid state at T^*. For example, NiAl with the off-stoichiometric composition 45:55 Ni:Al, is assumed to have the same enthalpy as stoichiometric NiAl, 50:50 Ni:Al and the appropriate amount of pure solid aluminum:

$$\Delta H(Ni_{0.45}Al_{0.55}, T^*) = 0.45\ \Delta H(NiAl, T^*) + 0.10\ \Delta H(Al, T^*). \qquad (3.4)$$

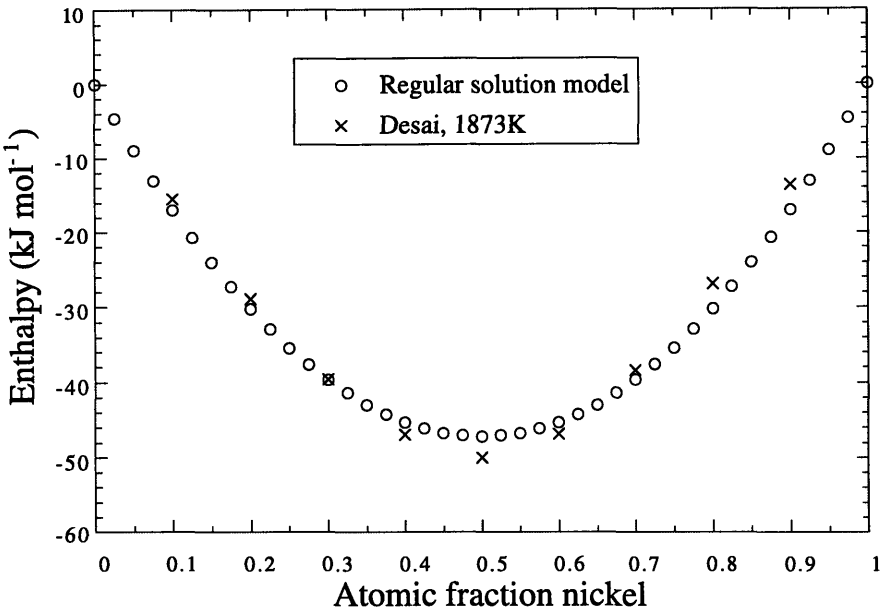

Fig. 3.1. Mixing enthalpy in the Al-Ni system for the regular solution model with Ω_{mix} = -189 kJ·mol^{-1} and for the data recommended by Desai at 1873K [61]. (Note that the standard state is the enthalpy of the pure liquids at the appropriate temperature.)

3.2. Enthalpy of the liquid

Significant heat is released when liquid aluminum and nickel are mixed. Using data recommended by Desai for the heat of mixing in the Al-Ni system at 1873K [61], and assuming the regular solution model the enthalpy of mixing Ω_{mix} was calculated. The enthalpy of the liquid, $\Delta H_{Al(Ni)}$ (written here as a solution of liquid aluminum, both by convention and because aluminum is less refractory), takes the form:

$$\Delta H_{Al(Ni)} = \overline{N}_0 \, \Delta H_{Al(l)} + (1 - \overline{N}_0) \, \Delta H_{Ni(l)} + \overline{N}_0 (1 - \overline{N}_0) \, \Omega_{mix} \qquad (3.5)$$

where $\overline{N}_0$ is the concentration of aluminum in the liquid expressed in mole fraction; $\Delta H_{Al(l)}$ and $\Delta H_{Ni(l)}$ are the molar enthalpies of the pure liquid aluminum and nickel respectively, calculated from data in Ref. [60], using the

same reference state as for the pure solid phases (*i.e.*, the elements in their standard state at 298K); and Ω_{mix} is the temperature-independent enthalpy of mixing, equal to -189 kJ·mol^{-1}. The data directly recommended by Desai at 1873K agree relatively well with values derived using eqn. (3.5), Fig. 3.1. (For simplicity, the reference states in Fig. 3.1 are taken to be the pure liquid elements at the appropriate temperature, *i.e.*, only the mixing term is plotted).

3.3. Adiabatic temperature

The adiabatic temperature (T_{ad}), frequently used in the analysis of SHS processing, is defined as the maximum temperature that can be reached in a reacting system assuming all the energy of reaction is available for heating the system (in other words, assuming the reaction is adiabatic). This value is typically reported with reference to 298K, although in what follows the term adiabatic temperature will be used with reference to some specified temperature T_i.

Consider the reaction A + B $\rightarrow$ C for a reaction product which undergoes only one change of state (generally melting) at temperature T_1. The adiabatic temperature for this reaction is calculated as:

$$\text{(i) if } T_{ad} < T_1, \quad \Delta_r H(298K) = \int_{298K}^{T_{ad}} Cp_C(T)\, dT \tag{3.6a}$$

$$\text{(ii) if } T_{ad} = T_1, \quad \Delta_r H(298K) = \int_{298K}^{T_1} Cp_C(T)\, dT + g_t\, \Delta_t H_C(T_1) \tag{3.6b}$$

$$\text{(iii) if } T_{ad} > T_1, \quad \Delta_r H(298K) = \int_{298K}^{T_1} Cp_C(T)\, dT + \Delta_t H_C(T_1) + \int_{T_1}^{T_{ad}} Cp_C(T)\, dT \tag{3.6c}$$

where $\Delta_r H(298K)$ is the standard enthalpy of the reaction at 298K; $Cp_C(T)$ is the specific heat capacity of the product phase C as a function of temperature in the appropriate temperature range; g_t is the fraction C transformed (melted), $\Delta_t H_C(T_1)$ is the enthalpy of the relevant phase transformation of the product C at T_1 [2]. This equation can be expanded to take into acount additional phase changes or reaction product phases.

Graphically the adiabatic temperature can be determined by plotting the enthalpy of the reactants and the enthalpy of the products as functions of temperature, *i.e.*, as given by eqn (3.3). Enthalpy functions of this type are plotted in Fig. 3.2 for stoichiometric NiAl, and for the sum of pure nickel and aluminum. The steps in the curves represent the melting of aluminum at 934K, of nickel at 1728K, and of the intermetallic (NiAl) at 1912K. The maximum temperature upon formation of NiAl from its elements at any initial temperature T_i can be determined from these curves by following the horizontal line (*i.e.*, constant enthalpy) from the enthalpy function of the reactants (Ni + Al) at T_i to the enthalpy function of the product.

This figure shows that at all starting temperatures greater or equal to 298K, the melting temperature of NiAl, 1912K, is reached or exceeded. Fully molten NiAl is formed if T_i exceeds 920K, a temperature very near the melting point of aluminum. Above the melting point of aluminum, T_{ad} of NiAl increases rapidly; for example, the adiabatic reaction of equal moles of nickel and aluminum at 973K (700°C) produces fully molten NiAl at 2114 K.

Fig. 3.3 shows the same information for the formation of stoichiometric Ni_3Al. Ni_3Al does not melt congruently, but experiences peritectic decomposition at 1668K and forms a fully liquid state at a slightly higher temperature. Thus, for simplicity, the transition from solid Ni_3Al to the fully liquid Al-Ni mixture (75 atomic percent nickel) is plotted as a dotted line on this figure. It is apparent from the figure that significantly lower temperatures are reached in the adiabatic formation of Ni_3Al: for initial temperatures below ~1000 K, the product is only partially molten.

3.4. Enthalpy of mixing/dissolution

The mixing enthalpy term in eqn (3.5) has a maximum value, -47 $kJ \cdot mol^{-1}$ at 50 atomic percent (a/o) nickel, Fig. 3.1; this is comparable to the standard enthalpy of formation of NiAl, -58 $kJ \cdot mol^{-1}$, Fig. 3.2. Assuming that the amount of nickel that will dissolve into liquid aluminum at a given temperature is determined by the liquidus lines of the phase diagram, Fig. 2.1, it is obvious that aluminum and nickel only mix in this ratio above the melting point of NiAl, 1912K. At lower temperatures, the effect of dissolution can be approximated by considering a system of pure nickel and molten aluminum saturated with nickel according to the phase diagram; the

enthalpy of this hypothetical system will be called the mixing enthalpy function.

Details of the enthalpy functions from Fig. 3.2 and 3.3 are show in Fig. 3.4 and 3.5 with the addition of the mixing enthalpy function plotted as a dotted line. The mixing enthalpy function for the equimolar system, Fig. 3.4, decreases with temperature between 933K and 1200K. This is due to the relatively large fraction of nickel in the system that must be dissolved at temperatures near the melting point of aluminum to achieve the liquidus composition. The enthalpy of mixing from this dissolution process significantly reduces the enthalpy of the system, creating a local minimum in the mixing enthalpy function. This situation is locally unstable as is the melting of nickel in this system: generally, melting requires energy input, but here the melting of nickel produces a net heat release due to the large mixing enthalpy, as shown by the discontinuous reduction in the enthalpy function at the melting point of nickel, 1728K. For this reason, a system of equimolar solid nickel in contact with pure liquid aluminum will tend to heat up spontaneously by dissolution of nickel at a high rate since the dissolution is limited only by diffusion in the liquid aluminum phase. In fact, equilibrium dissolutive mixing (above the melting point of aluminum in an adiabatic equimolar system) is energetic enough to produce molten NiAl above 1912K.

In the 75 a/o nickel system, on the other hand, the mixing enthalpy function increases continuously, Fig. 3.5. In this case, the fraction of nickel that must dissolve to maintain equilibrium is relatively small, *i.e.*, the heat capacity of the system is large due to the relatively large amount of nickel compared to aluminum. There are no local minima in the mixing enthalpy function; however, the system becomes complicated at temperatures near the eutectic and peritectic temperatures on the nickel-rich side of the phase diagram. Nevertheless, a system of 75 a/o nickel at an initial temperature of 1200K can thermodynamically transform into a system of pure nickel and aluminum saturated with nickel at a temperature of only about 1600K.

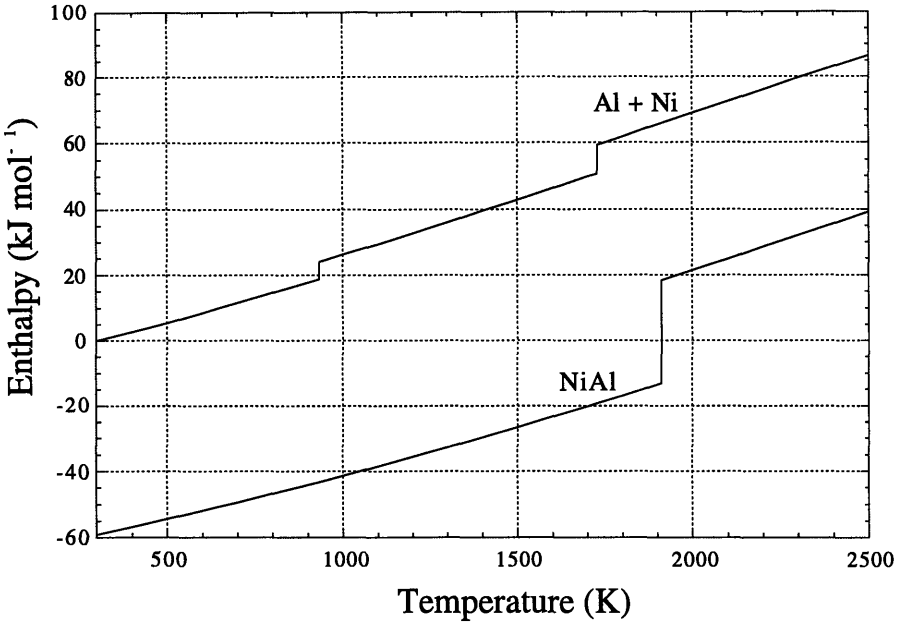

Fig. 3.2. Enthalpy functions for the reaction: 0.5 Al + 0.5 Ni → 0.5 NiAl

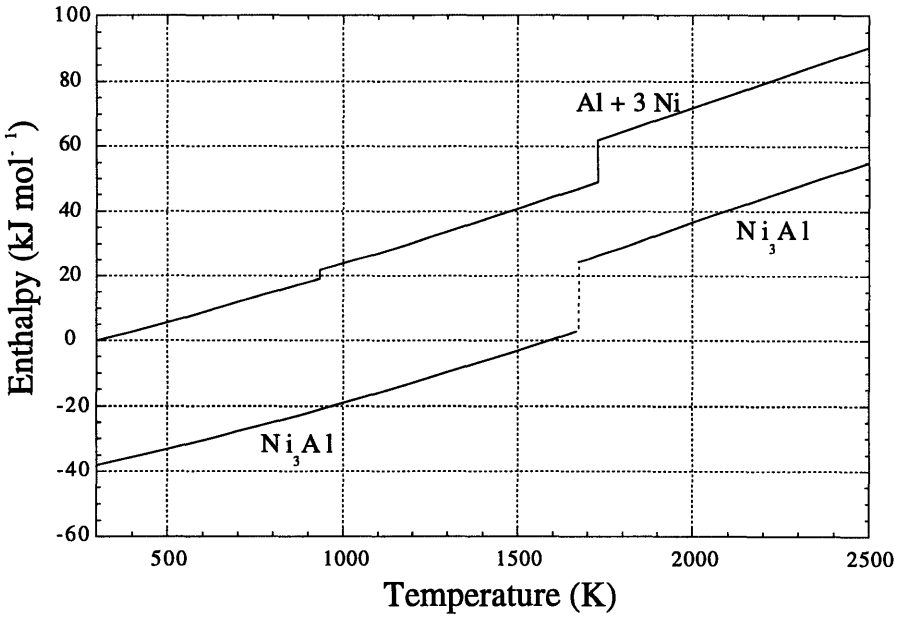

Fig. 3.3. Enthalpy functions for the reaction: 0.25 Al + 0.75 Ni → 0.25 Ni_3Al

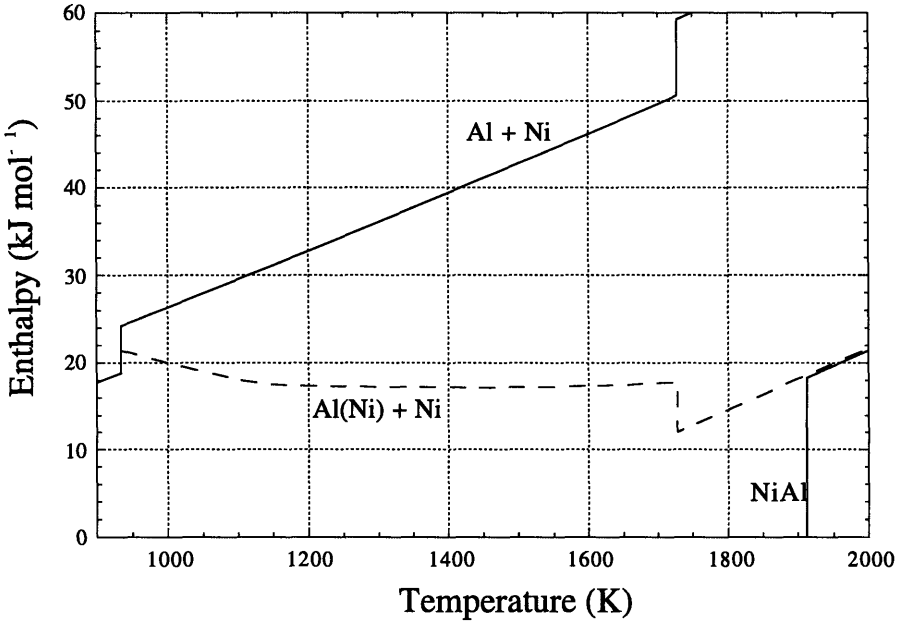

Fig. 3.4. Enthalpy functions for equilibrium mixing of 50 a/o nickel and the formation of NiAl.

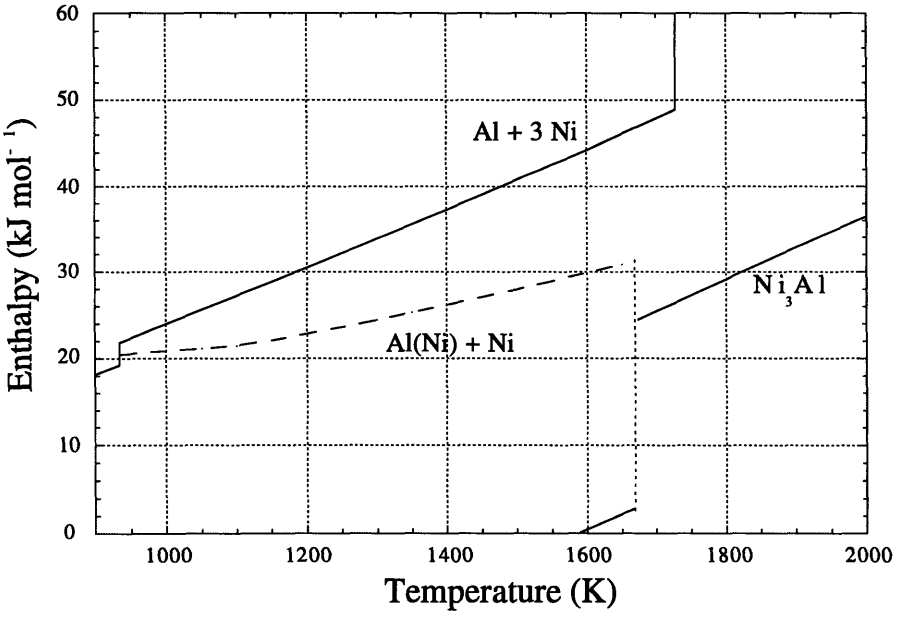

Fig. 3.5. Enthalpy functions for equilibrium mixing of 75 a/o nickel and the formation of Ni_3Al.

4. Experimental Procedures and Apparati

4.1. Materials and sample preparation

Fig. 4.1 shows the main elements of the as-prepared sample: the crucible, nickel preform, molten metal gate, and aluminum billet (before melting). The crucible material, quartz, was chosen for its resistance to thermal shock and its low cost; crucibles can be made in-house from inexpensive stock of various diameters up to ~2.5 cm. Although quartz softens near the melting point of NiAl [62], once infiltration is complete the crucible experiences nominal hydrostatic pressure. Since infiltration times are short, the crucible was found to maintain its structural integrity.

A chemical barrier was required to isolate the quartz, because aluminum rapidly reduces silica. Zircwash, a zirconia (ZrO_2) slurry for use as a mold coating (Zircwash, Zyp Coatings, Inc., P.O. Box 208, Oak Ridge, TN 37831, 615 482 5717), was therefore applied to the quartz crucible inner walls. Zircwash does not stick to quartz; thus, to obtain a uniform coating, the slurry was poured into the quartz crucible and the quartz was turned along its centerline on a lathe while air was blown into the crucible. When the slurry was dry to the touch, the coated crucible was placed in an oven at 150-200°C for several hours to complete drying. Crucibles used in high-speed digital imaging experiments were only coated on the upper-half of the crucible, such that the length of the nickel preform was visible, while the molten aluminum never contacted the quartz before pressurization.

Nickel wire preforms were created by wrapping wire around a card, then shearing the edges of the card to the desired length to produce wires of uniform length, generally between four and five centimeters, that could be collected in a bundle of aligned wires. Wires of 380 μm and 1000 μm diameter were obtained from Alfa Aesar (Johnson Matthey, Alfa Aesar, 30 Bond Street, Ward Hill MA 01835) with purity of 99.5%. Although theoretically the packing density of aligned close-packed cylinders is greater than 70% by volume, practically it is difficult to achieve packing densities greater than 45-50% because of the ductility of the wires; even small bends in the wires dramatically reduce the packing efficiency, but allow wire preform densities to be easily varied within the range of 20-40% by volume. So as not

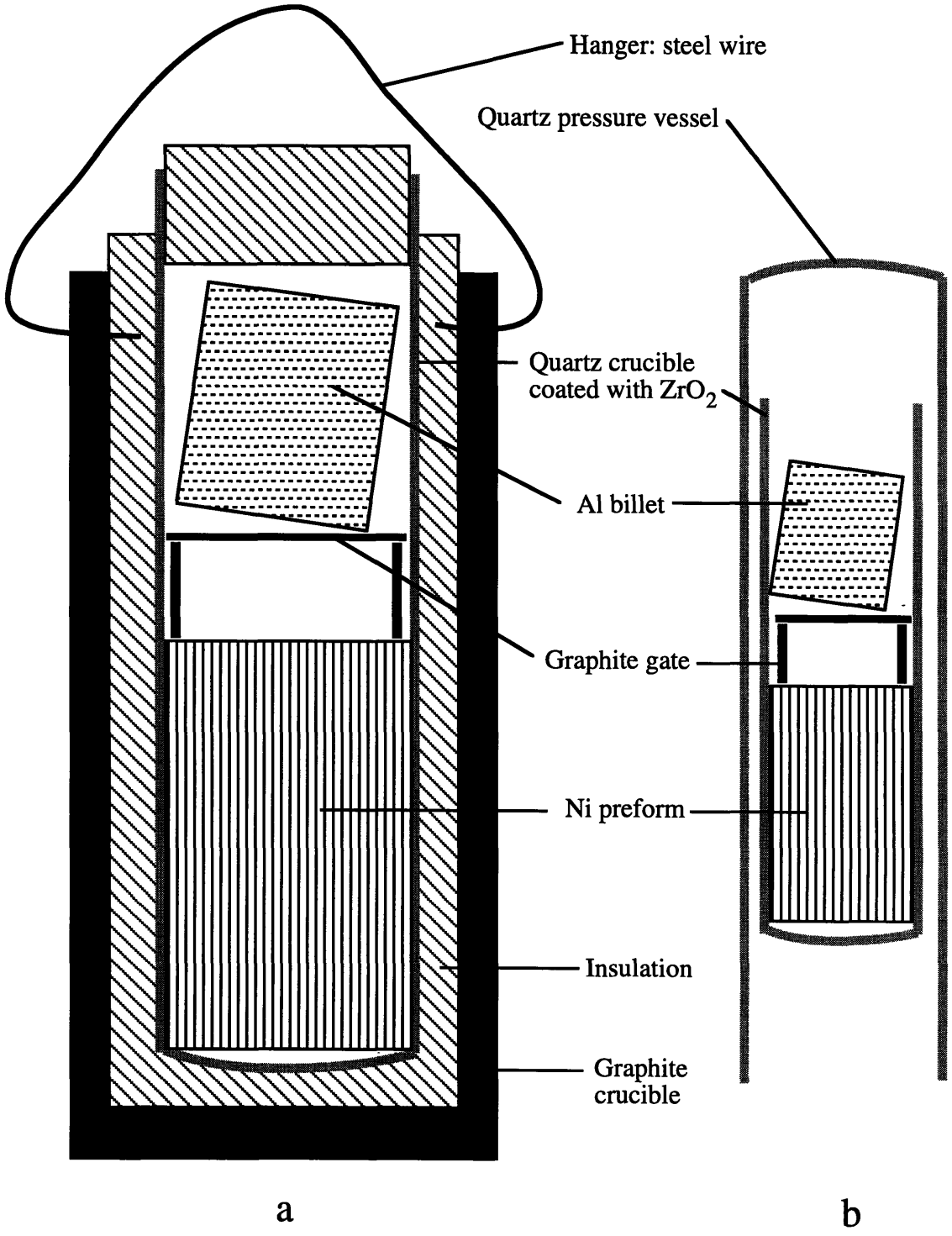

Fig. 4.1. Schematic of the crucible setup: (a) sample for the high-pressure system with 1.4x1.6 cm diameter crucible; and (b) sample for the low-pressure system with 2.5x2.7 cm diameter crucible.

to damage the zirconia coating on the crucible, the wire bundle of appropriate final density was forced into a metal tube that fitted easily into the crucible. The metal tube was then inserted into the crucible and the preform was extracted from the tube using a rod.

The aluminum had to be separated from the nickel preform until infiltration was initiated, lest reactions with the preform at unknown stoichiometry preclude a successful reaction sequence. A gate system was developed such that the molten aluminum flowed through the gate without significantly limiting the flow, thus insuring fast unidirectional infiltration. The gate system consisted of two parts: a graphite filter and a graphite reservoir, Fig. 4.2. The filter was simply a thin graphite disk with a diameter slightly smaller than the inner diameter of the crucible. Holes were drilled into the disk; these were small enough that capillarity would prevent liquid aluminum from flowing under the influence of gravity through the holes, yet numerous enough that the permeability of the gate was greater than that of the preform. Although larger holes could have been used, 0.035 inch holes (drill #65) were used, spaced evenly at a density of greater than 5 holes·cm^{-2} (*i.e.*, over 100 holes in a 2.5 cm diameter disk). The reservoir was a hollow thin-walled graphite cylinder ~1 cm in height with an outside diameter about the same as the filter. The reservoir distributed the flow of aluminum into the preform so that the preform was infiltrated uniformly across its cross-section, and hence unidirectionally. Both the filter and the reservoir were reusable.

The aluminum was cast into rods of appropriate diameter from 99.9% aluminum (Alcoa) billet. The aluminum rods were then cut to approximately the desired length, ground to the necessary weight, and placed in the crucible on top of the graphite gate system, Fig. 4.1.

4.2. Infiltration apparati and process parameters

4.2.1. High-pressure system

The high-pressure apparatus consisted of a thick-walled steel pipe with water cooled threaded caps, the top cap having a feedthrough for a 1/8 inch sheathed thermocouple and a 1/4 inch fitting connected to a manifold for applying vacuum, delivering the pressurized gas and venting, Fig. 4.3. The

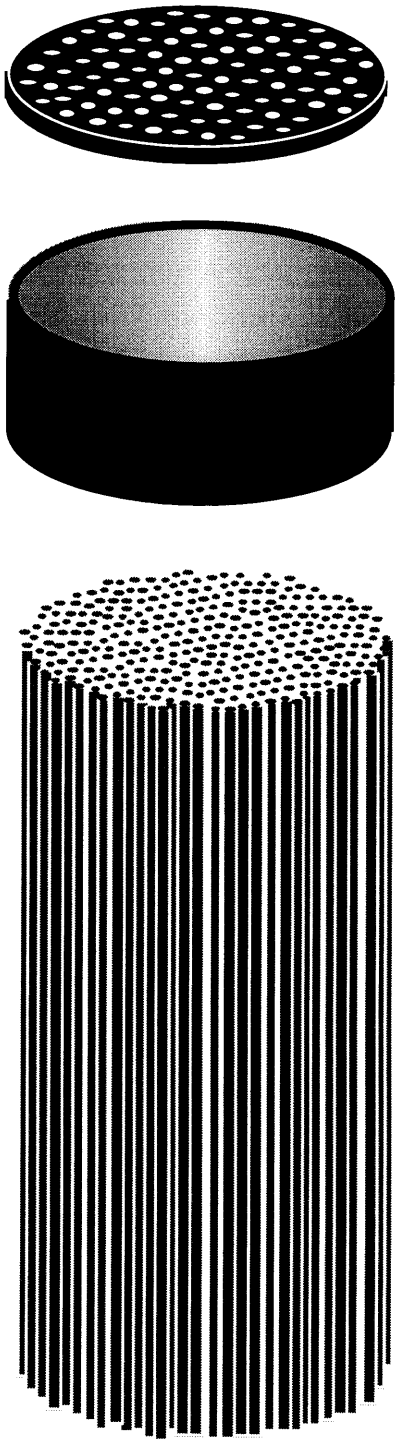

Fig. 4.2. Expanded isometric view of preform, graphite reservoir and graphite filter.

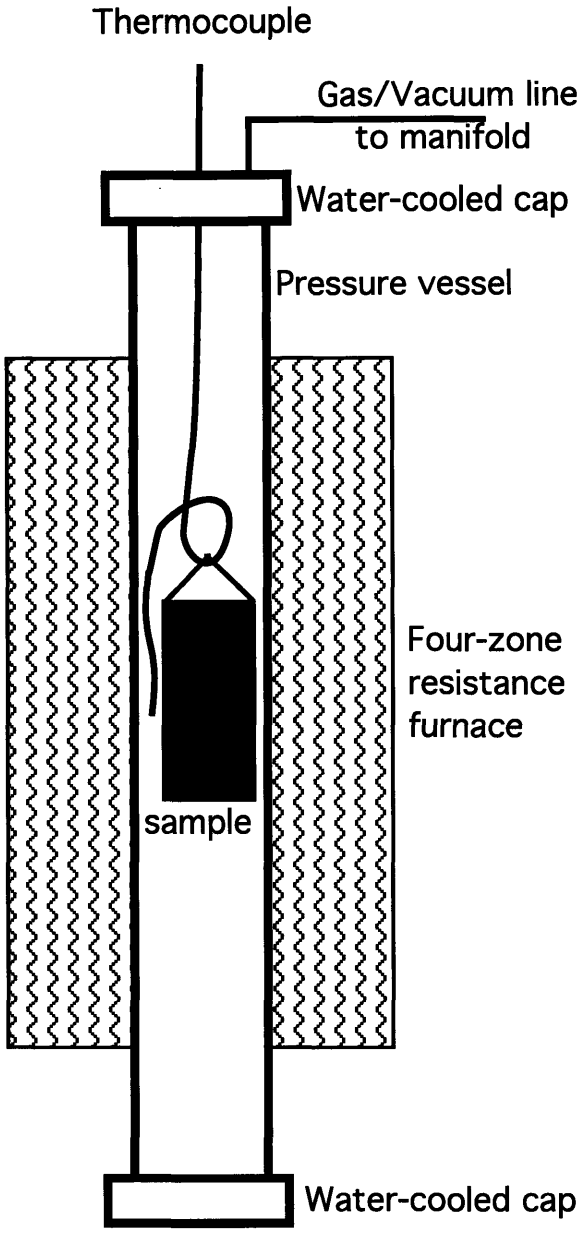

Fig. 4.3. Schematic of experimental high-pressure apparatus for reactive infiltration.

mid-section of the tube was heated externally by a series of cylindrical resistance furnaces. The pressure vessel could be heated to 700°C under vacuum and backfilled with inert gas up to 1000 psi.

The sample itself was suspended in the hot zone of the pressure vessel in a graphite crucible that was hung from a loop in the thermocouple probe by a

steel wire passing through holes at the top of the graphite crucible, Figs. 4.1a and 4.3. The sample crucible was wrapped in Fiberfrax® insulation paper (The Carborundum Company, Fibers Division, Niagara Falls NY 14302) and fitted snugly into the hanging graphite crucible with the tip of the thermocouple resting outside the graphite, level with the middle of the preform. The purpose of the graphite crucible was threefold: to provide a secure mechanical method of holding the sample crucible, to contain any spills due to failure of the sample crucible, and to act as a thermal sink after the reactions have gone to completion.

The 4.5-5.0 cm long wire preform was assembled in ZrO_2-coated quartz crucibles 2.5x2.7 cm in diameter, as described in section 4.1, placed into the pressure vessel, and heated to 700°C under a vacuum of less than 1 torr. The heating cycle was 2-3 hours, followed by pressurization (*via* manually operated valves) with argon at 30 psig for 5-60 minutes. Generally, the pressure was released after the temperature of the thermocouple dropped to less than 600°C. The sample, however, was not removed until the apparatus had cooled to below 200°C, after about three to four hours.

4.2.2. Low-pressure system

In place of the large thick-walled steel vessel, the low-pressure system employed a quartz tube as the pressure vessel, Fig. 4.4. This tube was closed at one end, of 1.7 and 1.9 cm inner and outer diameters respectively, and fitted into an ultra-torr fitting connected to a manifold. This allowed the pressure vessel to be moved in and out of a hot, vertically aligned, single-zone resistance tube furnace, which significantly reduced the heating cycle and turn-around time. As a consequence of the furnace orientation, however, significant axial temperature gradients existed.

The sample geometry and crucible did not differ from the high-pressure apparatus, with the following exceptions: (i) the preform was necessarily smaller, typically 4.0 cm long and 1.4 cm inner diameter; (ii) the sample crucible was not insulated; and (iii) the sample was held in place with a long thermocouple probe extending out of the hot zone to a feedthrough connected to the ultra-torr fitting. The system could be pressurized to 10 psig and the vacuum was generally about 500 mtorr. As in the high-pressure

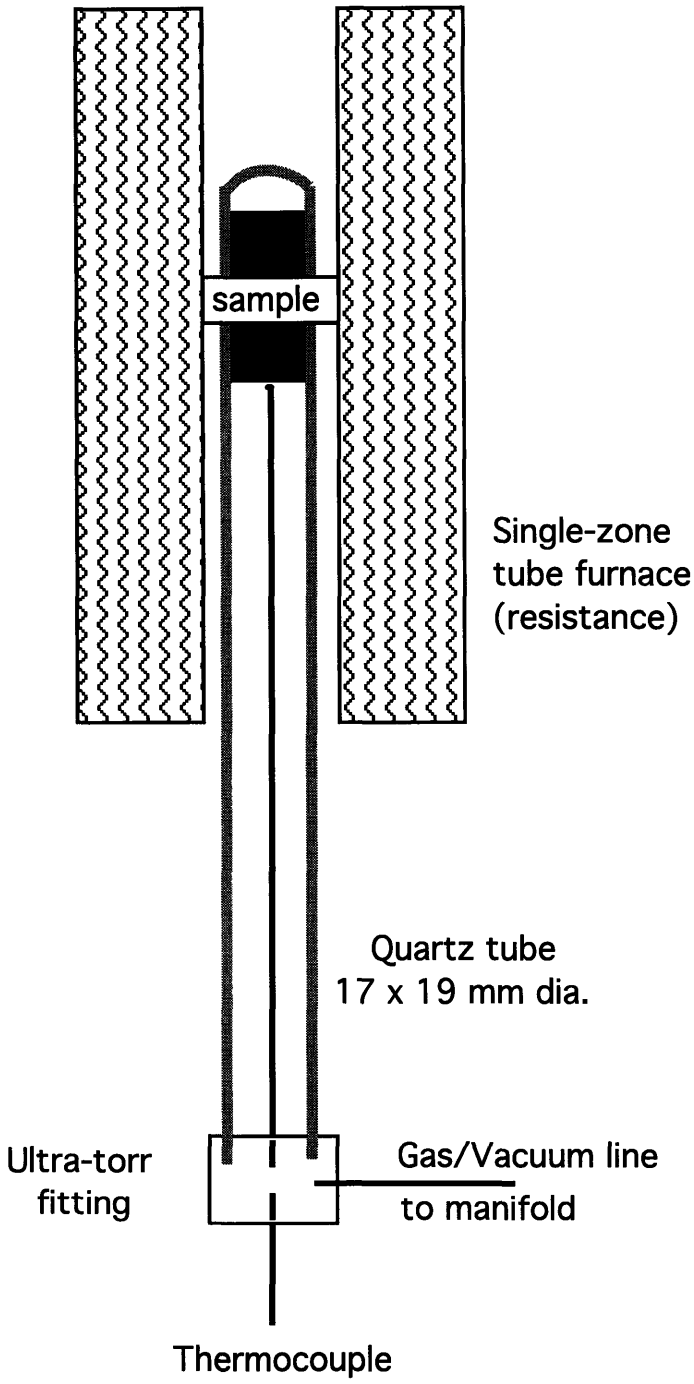

Fig. 4.4. Schematic of experimental low-pressure apparatus for reactive infiltration.

system, the crucible experienced nominal hydrostatic pressure after completion of infiltration, and showed no signs of deformation. On the other hand, the quartz pressure vessel was not under hydrostatic pressure, but showed no signs of deformation, presumably because it never reached temperatures greater than about 1200°C. On occasions, however, the quartz pressure vessel cracked due to violent expansion of the sample crucible whenever low-alloyed aluminum came into contact with exposed quartz.

Unlike experiments conducted using the high-pressure apparatus, samples could be inserted into the low-pressure apparatus and heated from room temperature to the infiltration temperature in a few minutes. After the samples were inserted into the quartz pressure vessel, the vessel was evacuated and then raised into the hot zone of the furnace, preheated to 800°C. Generally, the sample was left to reach thermal equilibrium with the furnace for 30-60 minutes, although the thermocouple holding the crucible in place reached 800°C in 10-15 minutes. The vessel was pressurized using manually operated valves to 6-10 psig argon for 1-2 minutes. The pressure was then quickly released to limit potential failure of the quartz vessel. The sample could be removed almost immediately (with due caution, considering its elevated temperature).

4.3. High-speed digital imaging

For high-speed digital imaging, the preform surface had to be exposed for observation. Thus, the low-pressure system was used and crucibles were half coated with zirconia such that the entire length of the preform was exposed, while the aluminum never contacted the exposed quartz crucible until pressurization. The clam-shell tube furnace was propped open with ceramic inserts, leaving a 0.5-1.25 cm viewing area for a Kodak EktaPro HS Motion Analyzer Model 4540 and a Kodak EktaPro 1000 camera. Both cameras collect and store digital images with 256 levels of gray that can be downloaded to a workstation or archived in analog format on conventional VHS format videotape. The EktaPro HS "camera" stores digital images of 256 by 256 pixels at up to 4500 frames per second (fps) and has the capability of storing smaller images at rates up to 40,500 fps. This camera was used to capture the reaction sequence at 125 fps; a low-band width optical filter (532 nm with an approximately 1 nm width) was used to reduce the intensity of the emitted

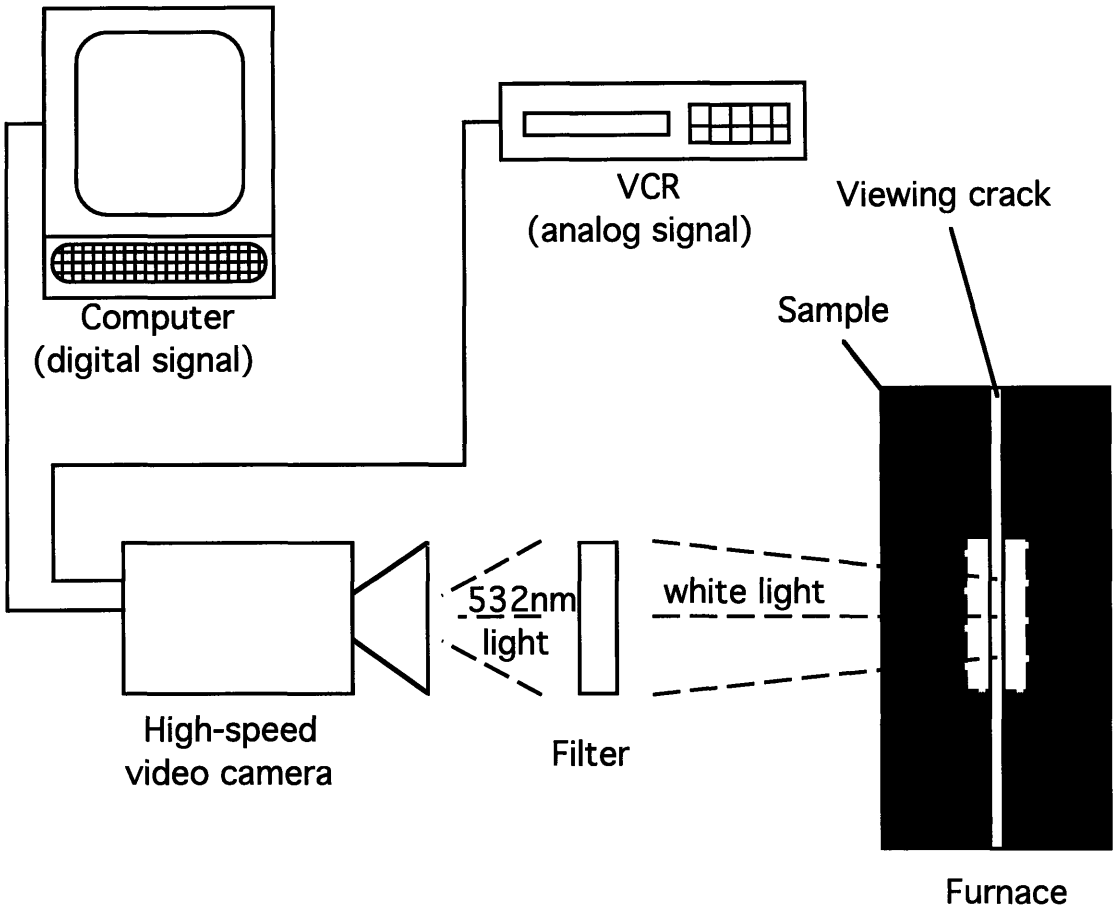

Fig. 4.5. Schematic of the high-speed digitized image acquisition system for low-pressure reactive infiltration.

light and to protect the sensing elements, Fig. 4.5. The EktaPro 1000 can store similar images at rates up to 1000 fps and was used without an optical filter to capture the infiltration sequence.

Preform preparation and infiltration procedures for the high-speed digitally imaged experiments were identical to those otherwise used for the low-pressure system, except that a solenoid valve initiated pressurization/infiltration so that the electronic signal could be used to trigger the EktaPro HS Motion Analyzer.

Henceforth, for simplicity, digital images and digitally imaged experiments will be referred to as video and video experiments respectively, even though video *sensu scricto* implies an analog format.

4.4. Sample characterization and signal processing

As-reacted samples were cut axially with a SiC abrasive wheel and polished with alumina suspensions. Often, the samples were not polished, since completeness of reaction, homogeneity, and phases present could be identified on as-cut cross sections. This was aided, for NiAl, by the fact that there is a sharp minimum in the diffusion coefficient near 50 atomic percent [8, 63, 64], such that transitions from nickel-rich NiAl, yellow to gold in color, to aluminum-rich NiAl, white to blue in color, were relatively abrupt. Some samples were etched for a few seconds to enhance the contrast between NiAl and Ni_3Al (by submersion in a solution of 1 g $CuCl_2$, 20 mL HCl, and 20 mL ethanol).

The digitally recorded data are presented in several ways. The simplest method used was creating a composite of the images, as collected, or with false-contrast and/or color to emphasize the intensity changes. Quantitative data analysis was performed using scripts in IPLab Spectrum software for the Macintosh (Signal Analysis Corporation, Suite 201, 440 Maple Ave. East, Vienna VA 22180), including intensity presentations and reaction front tracking. A single pixel (corresponding to a fixed position in the sample) was tracked, plotting the intensity as a function of time (measured by image frame number). These data represent the local emission history at the surface of the sample, and are directly related to the thermal history of the local position along the sample surface.

As will be shown below, combustion fronts were observed in the reacting Al-Ni samples. These were easy to locate using local emission history data as a rapid increase in the intensity of emission with respect to time, stable steady propagation being manifest by the presence of equidistant intensity curves for equidistant positions.

In the second method, the velocity of the combustion front was determined by identifying the position of the sudden rise in light emission with time. An intensity, called the segmentation intensity, was identified that distinguished the combustion front and each pixel in the image was analyzed to determine whether it was segmented (greater than or equal to the segmentation intensity) or unsegmented (less than the segmentation intensity). By plotting the position of the sharp transition between the

Table 4.1. Vendor supplied powder specifications

Vendor and product number	diameter range (μm)*	apparent density ($g \cdot cm^{-3}$)	powder morphology
Sherritt 7111	150-180	4.4	spheroidal
Sherritt 7131	106-150	4.2	spheroidal
Sherritt 7181	20-45	3.6	spheroidal
Sherritt 6211	0.7-1.4	1-2	spheroidal
Novamet 4SP	3.9-44	3.0	spheres

* More than 90 wt % of the powders are within the specified range.

segmented and unsegmented regions for a sequence of images, the velocity of the combustion front was determined.

4.5. Additional experiments

4.5.1. Other preform morphologies

Nickel preforms from powder provided by Sherritt (Sherritt Technologies, Specialty Materials, Fort Saskatchewan, AB, Canada T8L 3W4, 403 992 5026) were created by gently tamping the powder directly into the crucible with a rod. The apparent density and powder sizes as supplied by the vendor are listed in Table 4.1. Porous nickel pieces (Cerac, Inc., 407 North 13th St., Milwaukee WI 53233) were also used as preform materials; these were simply poured into the crucible. These pieces had a maximum dimension of up to one inch, but were specified as 1/8 inch pieces by the vendor, presumably meaning that the pieces had a minimum dimension of at least 1/8 inch.

4.5.2. "Filter" experiments

Several experiments were performed whereby aluminum was flushed through a nickel preform, such that the "filtered" aluminum could be collected for analysis. These experiments were done in the high-pressure apparatus as described above, except that the preform was held above the

bottom of the crucible by a graphite filter and ceramic posts. This type of experiment produced a small quantity of aluminum that had traversed the entire sample length, which was collected from the reservoir below the preform and analyzed to assess the level of nickel dissolution by the flowing aluminum during infiltration.

4.5.3. "Vacuum" experiments

Experiments in the low-pressure apparatus were also performed by applying vacuum to a system heated under pressure, rather than applying pressure to an evacuated system. The term "vacuum" experiments will be used to differentiate this type of experiment from the others. The sample configuration was inverted in the crucible such that the aluminum was at the closed end of the crucible, and the preform at the open-end with the same gate system separating the aluminum from the preform. The molten intermetallic does not wet aluminosilicates at low pressures, therefore, a porous plug of aluminosilicate insulation was used to prevent the molten intermetallic from flowing out of the crucible during the reaction, while allowing gas to be evacuated from the preform during infiltration. The crucible was placed in the low-pressure apparatus (with the crucible inverted to leave the aluminum on top) and heated under an argon atmosphere pressurized to 6-10 psig. Vacuum was then applied, after appropriate heating, to create the necessary pressure differential across the liquid aluminum to drive the infiltration.

5. Experimental Results

5.1. Powder preform infiltration

Assuming no solute (nickel) transport during infiltration, a nickel preform filled with molten aluminum at 700°C requires a preform volume fraction V_p of 0.37 (apparent density of 3.3 $g \cdot cm^{-3}$) to form equiatomic NiAl. This volume fraction is difficult to attain with equiaxed powders, which generally pack to volume fractions in the vicinity of 0.55 to 0.65. Indeed, from vendor-supplied powder specifications, Table 4.1, it is apparent that the larger powders pack too densely, and that only fine powders, if green pressed or sintered, can form appropriate preforms.

Preforms of nickel powder (Sherritt 7111, Table 4.1) were infiltrated in the high-pressure apparatus at 1000 psig. Resulting samples featured a complex mixture of various intermetallic phases, Fig 5.1, separated into irregular bands, each of widely different compositions and relatively constant structure.

These preforms have permeabilities less than 10^{-5} cm^2 and pack to densities greater than required for stoichiometric NiAl. Because preforms packed with all other available powders listed in Table 4.1 feature lower permeabilities than Sherritt 7111 powder, these were not explored; instead, wire preforms of much higher permeability were used for all other experiments.

5.2. Wire preform infiltration

It was observed that RIP of wire preforms can be separated in time into three stages: (i) infiltration, (ii) incubation, and (iii) reaction. Infiltration was estimated to take place at velocities as high as 80 $cm \cdot s^{-1}$ using high-speed video, Table 5.1. The average rate of infiltration was measured using the digital camera without the optical filter such that the flowing metal could be observed, Fig. 5.2. No self-heating was observed during infiltration, thus, it is inferred that infiltration takes place without significant reaction in wire preforms.

Infiltration was followed by a period, called here incubation, lasting between 2 and 3 seconds, Table 5.1, and characterized by slow self-heating of

the sample. The nickel wire preform/liquid aluminum composite was observed to glow uniformly with increasing intensity until the video sensing elements were light-saturated. In experiments W1 to W4 the video camera and the infiltration were triggered independently, therefore, the incubation times in Table 5.1 are approximate for these samples.

Thereafter, a combustion wave was observed to initiate at the infiltration entrance (*i.e.*, at the top of the preform), Fig. 5.3, and to propagate through the nickel wire/liquid aluminum composite in the direction of infiltration, Figs. 5.4, 5.5 and 5.6. In one observed case, Sample W11, the combustion wave initiated near the middle of the preform, rather than at the top of the preform as observed in all other cases.

In several experiments, global collapse of the infiltrated sample was visible behind the reaction front as propagation progressed. This collapse, visible in Fig. 5.3, indicated that the hot reacted portion of the sample was fully molten. Other indications of the existence of molten material behind the combustion front include: (i) the development of a large bubble or void during reaction, Fig. 5.6, in electronically triggered video experiments (W7 to W16), and (ii) shifting bright spots in the hot region of the samples, resembling plumes of circulating fluid temporarily visible on the surface of the sample.

The bubbles typically formed near the middle of the preform length and occupied almost half the sample diameter. These experiments had viewing windows of about 1.25 cm, compared to ~0.5 cm for the manually triggered video experiments (W1 to W4), in which no large bubbles formed. The existence and formation of the large bubbles in the former experiments made interpretation of the quantitative data difficult, although qualitatively these experiments showed the same features as experiments W1 to W4; compare Figs. 5.4, 5.5, and 5.6. Therefore, two sets of experimental data are used to illustrate the salient features observed in the video record of all samples: (i) Sample W2 with 61 atomic percent (a/o) nickel, referred to as nickel-rich in the following analysis; and (ii) Sample W3 with 43 a/o nickel, referred to as aluminum-rich.

In the fourth image of the composite in Fig 5.4a, a bright region developed near the middle of the length of the sample. Fig. 5.4b shows this region, called here a "hot spot," with increased temporal resolution. "Hot spots" were only observed in experiments with nickel in excess of 50 a/o in the fully reacted zone behind the combustion front. Furthermore, they appeared to propagate

upwards, resembling plumes of rising convected hot fluid, during visual examination of the animated recorded images (unfortunately, still images as in Fig. 5.4 do not convey the motion observed in animated video segments). A corresponding set of intensity profiles are shown in Fig. 5.7 for Sample W2 where the initial rapid rise in intensity represents the position of the combustion front and the subsequent spike in intensity is the "hot spot" propagating upwards. Hot spots were absent from experiments with nickel compositions less than 50 a/o, such as Sample W3, Fig. 5.5, thus the corresponding intensity profiles, Fig. 5.8, do not show evidence of emission spikes as observed in the nickel-rich samples.

The velocity of the combustion front was relatively steady during the initial stages of propagation for all samples. In particular, the aluminum-rich sample, Fig. 5.8a shows quantitatively similar and equally spaced profiles initially, but the combustion front became unsteady soon thereafter, as shown in Fig. 5.8b by the spatial and temporal non-uniformity of the intensity profiles.

The velocity of the reaction wave in the initial steady propagation regime was determined from the video record using the segmentation procedure as outlined in Section 4.3. In general, the combustion wave front initially propagated with a steady velocity that later became non-steady as in Sample W4, or changed to a second lower steady velocity before becoming non-steady as observed in the other samples without the large bubbles. Figs. 5.9-5.12 show the wave front position with time in the steady propagation regime for experiments W1 to W4.

5.3. Sample macrostructure

Reacted nickel wire samples produced using 380 μm wires in the high pressure system at 700°C, Table 5.3, featured five different macrostructures depending on their global composition:

(i) NiAl with aluminum rich phases (Al-rich) are characterized by a layer of aluminum-rich material situated on top of a second zone of monolithic NiAl. At the top of the Al-rich region, there are Al_3Ni precipitates surrounded by eutectic material, Fig. 5.13a. Near the interface with NiAl, the Al-rich region contains dendrites of

Al_3Ni_2 surrounded by a layer of Al_3Ni and small amounts of eutectic material, Fig. 5.13b.

(ii) Monolithic NiAl (NiAl) regions contain only single-phase NiAl, Fig. 5.14, the composition of which is often seen to vary somewhat across the height of the sample within the wide NiAl phase field.

(iii) NiAl with nickel rich phases (Ni-rich) are composed of two main regions, Fig. 5.15, namely a layer of Ni_3Al at the bottom of the sample and a monolithic NiAl layer at the top, often with a region of two-phase NiAl-Ni_3Al material between these two larger regions.

(iv) "Free wire" samples featured a monolithic NiAl region with unreacted nickel wires remaining at the bottom of the sample that are at least partially infiltrated with nickel-rich material, Fig. 5.16.

(v) Finally, some samples featured a homogeneous structure of partially reacted nickel wires embedded in aluminum near-eutectic material with thin layers of the intermetallics after the phase diagram separating the two larger regions, namely the nickel-saturated aluminum and the pure nickel wire. These samples were, thus, essentially unreacted.

Nickel wire samples processed with the low-pressure system produced macrostructures qualitatively the same as in the high-pressure apparatus, for both digital video experiments, Table 5.3, and non-video experiments alike, Table 5.4. In addition, a preform of 1.0 mm diameter nickel wires was infiltrated, and reacted to form NiAl (Al-rich) in accordance with expected results for 380 μm wire samples.

These results are summarized in Fig. 5.17, which is a processing map that shows the dependence of the final structure on the nickel atomic fraction N_{Ni} for all the experiments with nickel wire preforms.

5.4. Additional experiments

5.4.1. Other preforms morphologies

Preforms packed using large nickel pieces described in Section 4.5.1 were infiltrated using both the high-pressure (Sample E65) and the low-pressure systems (all other samples), Table 5.5. These preforms reacted to produce

homogeneous bulk NiAl: for example, Sample W65, produced using a preform 7.8 cm in height by 2.5 cm in diameter (~150g), was infiltrated completely and reacted to form a block of homogeneous NiAl.

5.4.2. "Filter" experiments

Only small amounts of aluminum, less than 10% by weight of the initial aluminum charge, were collected by flushing aluminum through nickel preforms. Optical microscopy showed that the "filtered" material was hypo-eutectic. The aluminum infiltrate can, thus, traverse the entire length of wire preforms with relatively minimal nickel dissolution.

5.4.3. "Vacuum" experiments

Some of the best images were obtained using the vacuum setup, Fig. 5.2 and it produced samples that showed no discernible difference compared to the other setups. However, the intermetallic melt was difficult to contain, thus the vacuum setup was not used further.

Table 5.1. Summary of estimated infiltration rate, incubation time and steady-state combustion front velocity for digital video experiments

Sample ID	N_{Ni}	infiltration velocity ($cm \cdot s^{-1}$)	incubation time (s)	initial steady u ($cm \cdot s^{-1}$)	final steady u ($cm \cdot s^{-1}$)
W16	0.54	44	2.6	†	†
W15	0.74	40	2.6	†	†
W14	0.60	†	2.3	†	†
W11	0.54	80	3.3	---	1.9
W10	0.60	20	2.3	~2.8	~1.5
W9	0.69	13	∞	---	---
W8	0.59	28	3.2	2.8	~1.5
W7	0.64	---	∞	---	---
W4*	0.47	---	~1.6	---	1.2
W3*	0.43	---	~2.1	5.2	2.2
W2*	0.61	---	~1.8	4.8	3.4
W1*	0.70	---	~1.4	8.1	0.95

* not triggered electronically
† not determined

Table 5.2. Summary of high-pressure system experiments, 380 μm diameter nickel wire preforms, infiltrated at 700°C under 30 psig Ar

Sample ID	height (cm)	diameter (cm)	V_p	N_{Ni}	macro-structure
E63	5.0	2.44	0.37	0.44	Al-rich
E61	4.5	2.46	0.32	0.38	Al-rich
E60	4.5	2.44	0.32	0.43	Al-rich
E59	4.5	2.44	0.32	0.46	Al-rich
E56	4.5	2.46	0.24	0.76	free wires
E55	5.0	2.46	0.27	0.69	Ni-rich
E54	5.0	2.47	0.36	0.57	NiAl
E53	5.0	2.47	0.36	0.59	free wires
E52	5.0	2.47	0.36	0.61	NiAl
E51	5.0	2.47	0.36	0.68	Ni-rich
E50	5.0	2.47	0.36	0.62	free wires
E47	5.0	2.48	0.36	0.75	free wires
E45	5.0	2.47	0.26	0.49	Al-rich
E43	5.0	2.47	0.36	0.65	Ni-rich
E42*	5.0	2.44	0.37	0.51	Al-rich
E40	5.0	2.46	0.38	0.52	Al-rich

* 1 mm diameter wires

Table 5.3. Summary of digital video experiments, 380 μm diameter nickel wire preforms infiltrated at 800°C under Ar

Sample ID	height (cm)	dia-meter (cm)	pressure (psig)	V_p	N_{Ni}	macro-structure
W16	4.0	1.39	8	0.33	0.54	NiAl
W15	4.0	1.39	8	0.33	0.74	free wires
W14	4.0	1.39	8	0.33	0.60	NiAl
W11	4.0	1.39	8	0.33	0.54	NiAl
W10	4.0	1.39	8	0.33	0.60	NiAl
W9	4.0	1.39	8	0.44	0.69	unreacted
W8	4.0	1.39	8	0.44	0.59	NiAl
W7	4.0	1.39	8	0.43	0.64	unreacted
W4	4.0	1.40	9	0.32	0.47	Al-rich
W3	4.0	1.40	10	0.33	0.43	Al-rich
W2	4.0	1.40	9	0.32	0.61	NiAl
W1	4.0	1.40	10	0.33	0.70	Ni-rich

Table 5.4. Summary of low-pressure system experiments, 380 μm diameter nickel wire preforms infiltrated under 10 psig Ar

Sample ID	height (cm)	dia-meter (cm)	T_i (°C)	V_p	N_{Ni}	macro-structure
V27	3.8	1.38	---	0.36	0.52	Al-rich
V25	4.0	1.38	750	0.30	0.54	NiAl
V22	4.0	1.23	805	0.27	0.48	Al-rich
V17	4.5	1.37	833	0.23	0.41	Al-rich
V12*	4.5	1.38	---	0.33	0.58	Al-rich
V11*	4.0	1.37	825	0.32	0.40	Al-rich
V10*	4.0	1.38	840	0.30	0.39	Al-rich
V9*	4.0	1.38	825	0.34	0.53	NiAl

* 6 psig

Table 5.5. Summary of experiments with "1/8 inch nickel pieces," infiltrated under 10 psig Ar in the low-pressure system

Sample ID	height (cm)	dia-meter (cm)	T_i (°C)	V_p	N_{Ni}	macro-structure
E65*	7.8	2.46	700	0.34	0.50	NiAl
V29	5.0	1.38	835	0.28	0.66	NiAl
V28	5.0	1.37	700	0.29	0.63	Ni-rich
V26	4.4	1.38	755	0.32	0.52	NiAl
V23	5.3	1.27	---	0.28	0.72	free wires
V20	5.5	1.37	861	0.29	0.56	Al-rich
V19	5.1	1.37	862	0.30	0.44	Al-rich

* high-pressure system at 30 psig Ar

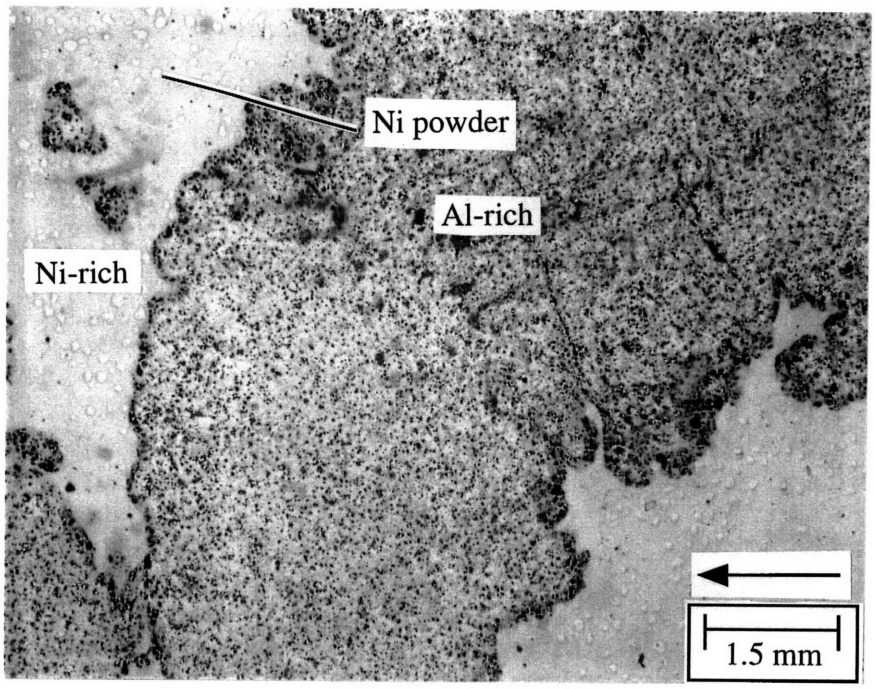

Fig. 5.1a. Optical micrograph of infiltrated nickel powder, showing the peneration of the grainy aluminum-rich phases (aluminum, Al_3Ni, and Al_3Ni_2) and the lighter nickel-rich phases (NiAl, Ni_3Al, and nickel powders). The arrow shows the direction of infiltration.

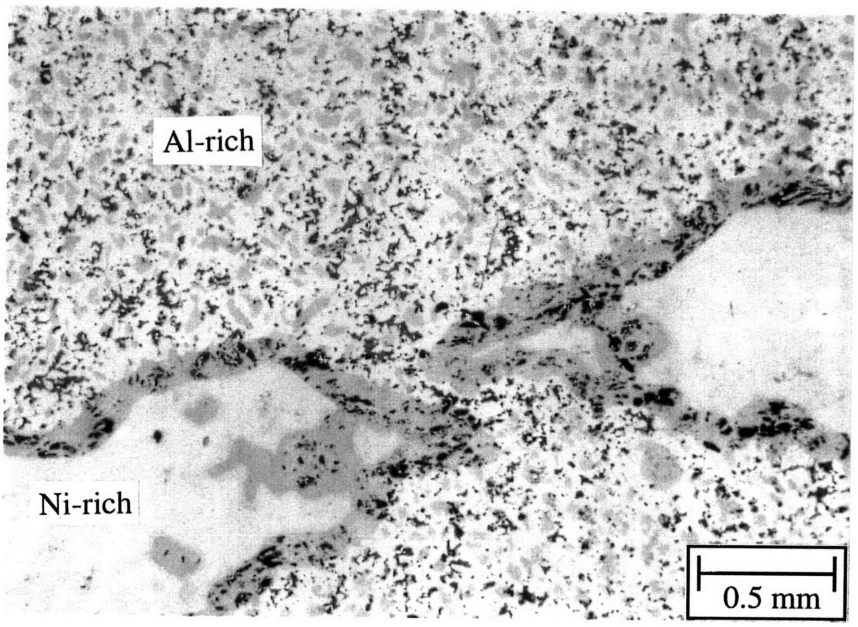

Fig. 5.1b. Higher magnification of Fig 5.1a, showing irregular regions of relatively uniform NiAl bounded by gray Al_3Ni_2 phase and Al-rich regions.

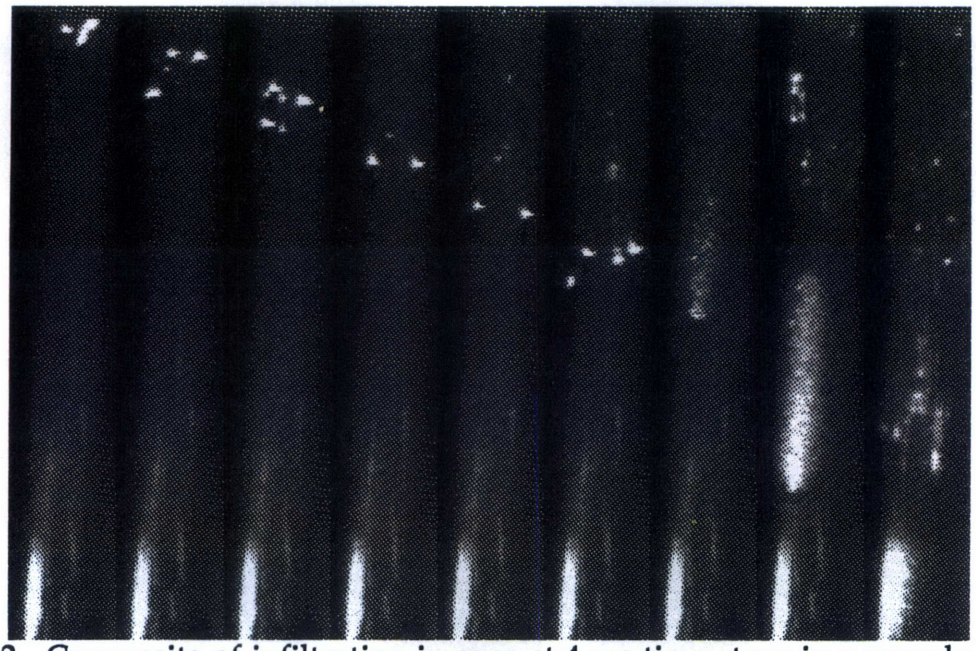

Fig. 5.2. Composite of infiltration images at 4 ms time steps in a sample processed by the "vacuum" technique. The initial infiltration features metal penetrating along narrow channels, while the final images show the metal filling the large pores along the crucible wall under the influence of the pressurized gas. (Viewing window width ≈ 0.5 cm.)

Fig. 5.3. False-color images of the initial stages of combustion at 40 ms time steps in Sample W10, N_{Ni} = 0.60. The combustion front ignites at the top of the preform forming a fully liquid region behind the combustion front. (Viewing window width ≈ 1.25 cm.)

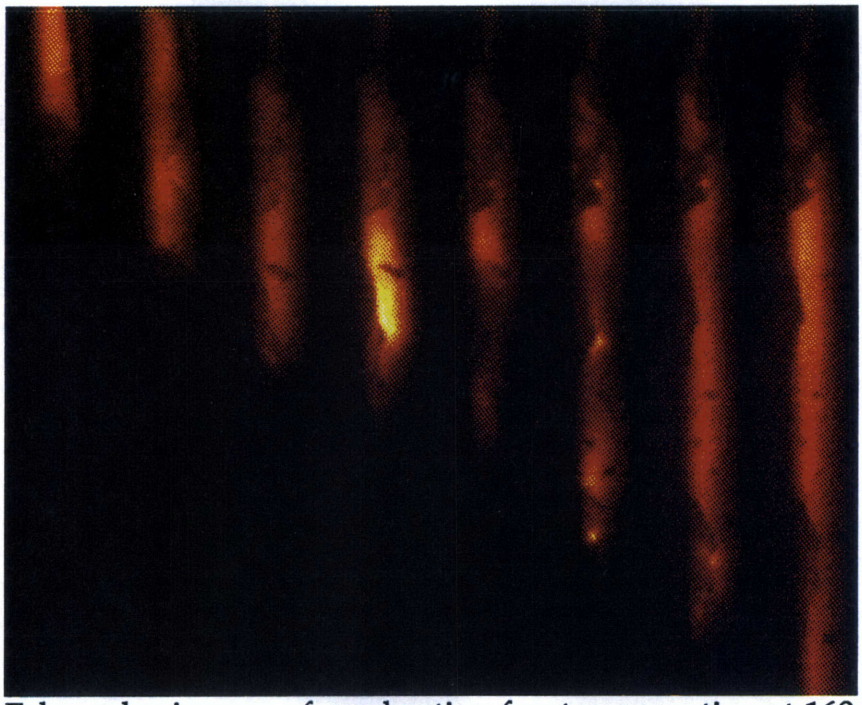

Fig. 5.4a. False-color images of combustion front propagation at 160 ms time steps in Sample W2, N_{Ni} = 0.61. A large "hot spot" can be seen in the fourth frame. (Viewing window width ≈ 0.5 cm.)

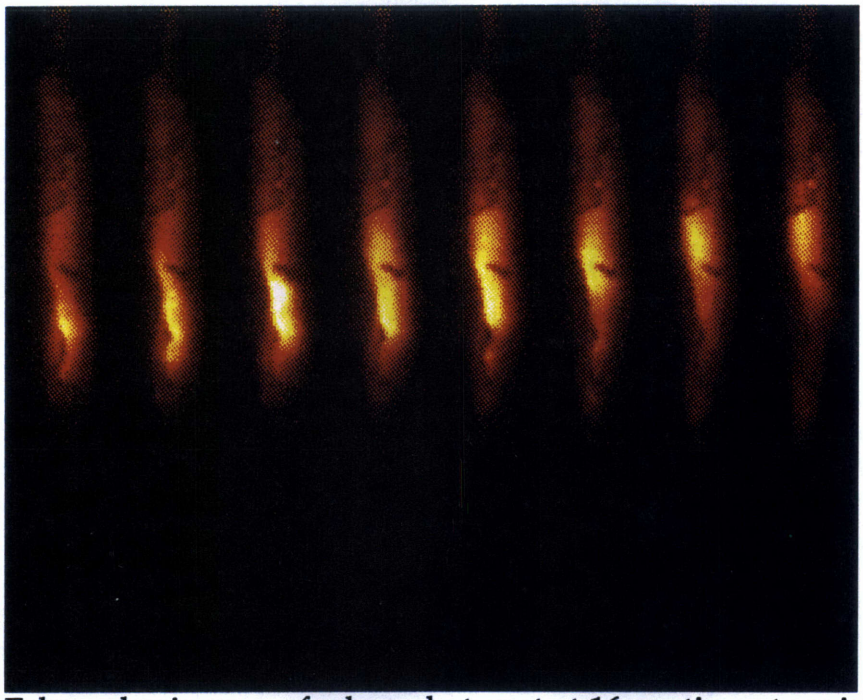

Fig. 5.4b. False-color images of a large hot spot at 16 ms time steps in Sample W2, N_{Ni} = 0.61, centered around the fourth image from Fig. 5.4a. The "hot spot" rises with time and cools. (Viewing window width ≈ 0.5 cm.)

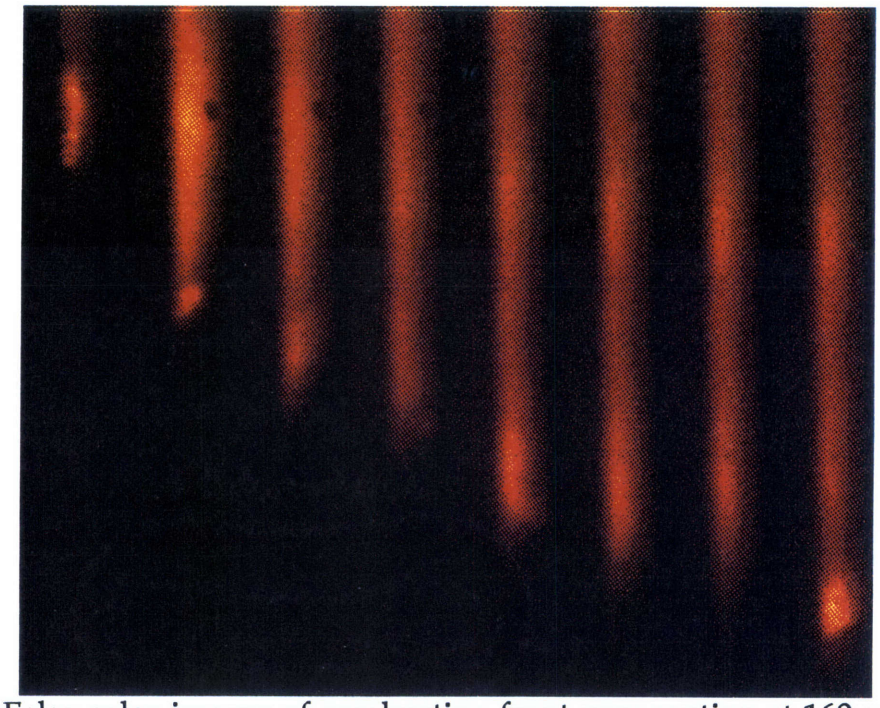

Fig. 5.5. False-color images of combustion front propagation at 160 ms time steps in Sample W3, N_{Ni} = 0.43. The intensity is uniform throughout the entire sample. (Viewing window width ≈ 0.5 cm.)

Fig. 5.6. False-color images of combustion front propagation and bubble formation at 320 ms time steps in Sample W10, N_{Ni} = 0.60. Note the areas of changing intensity and hot spots. (Viewing window width ≈ 1.25 cm.)

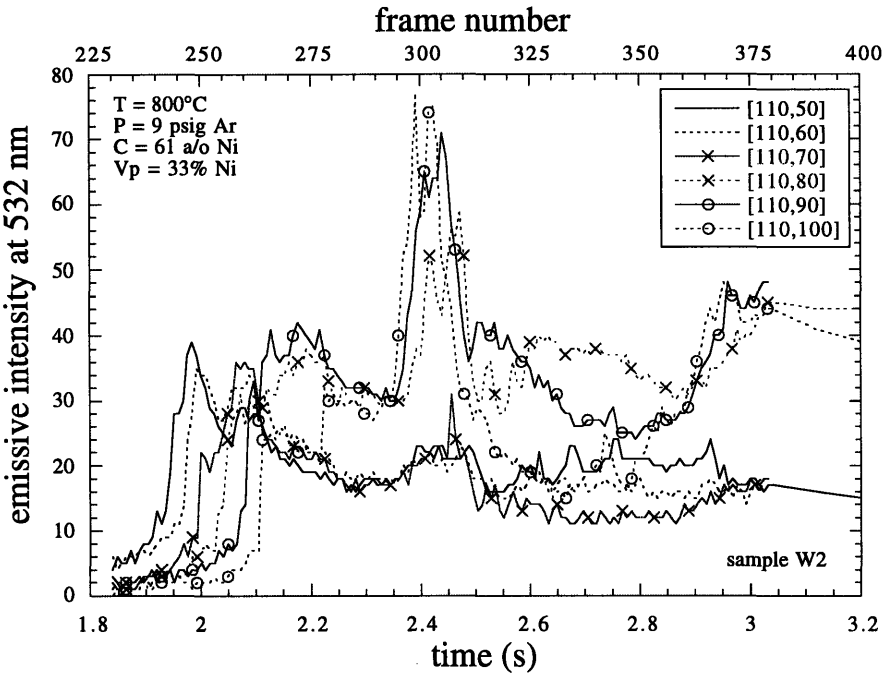

Fig. 5.7. Emissive intensity for Sample W2, N_{Ni} = 0.61. (79 pixels = 1 cm).

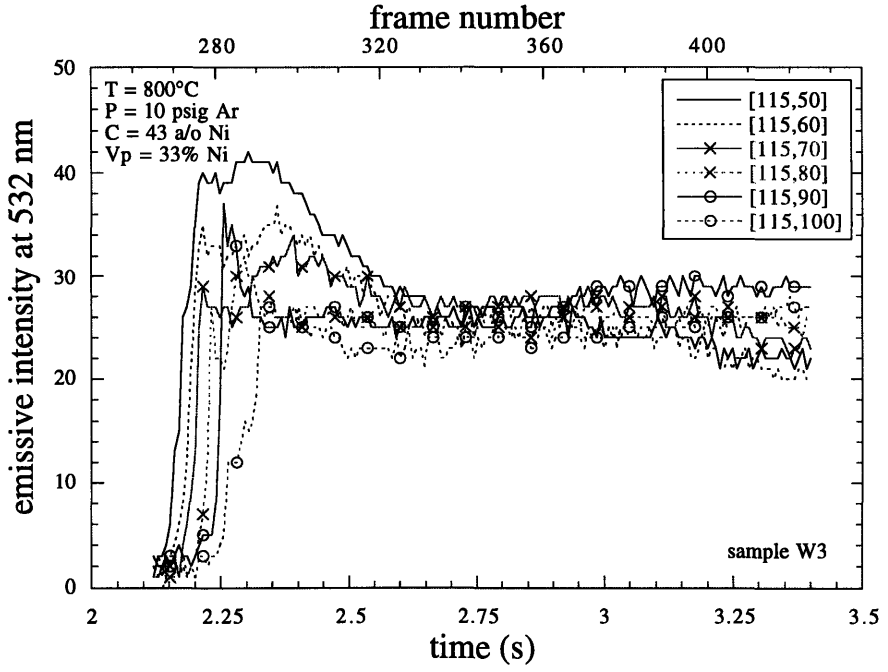

Fig. 5.8a. Emissive intensity for Sample W3, N_{Ni} = 0.43, in the steady propagation regime (79 pixels = 1 cm).

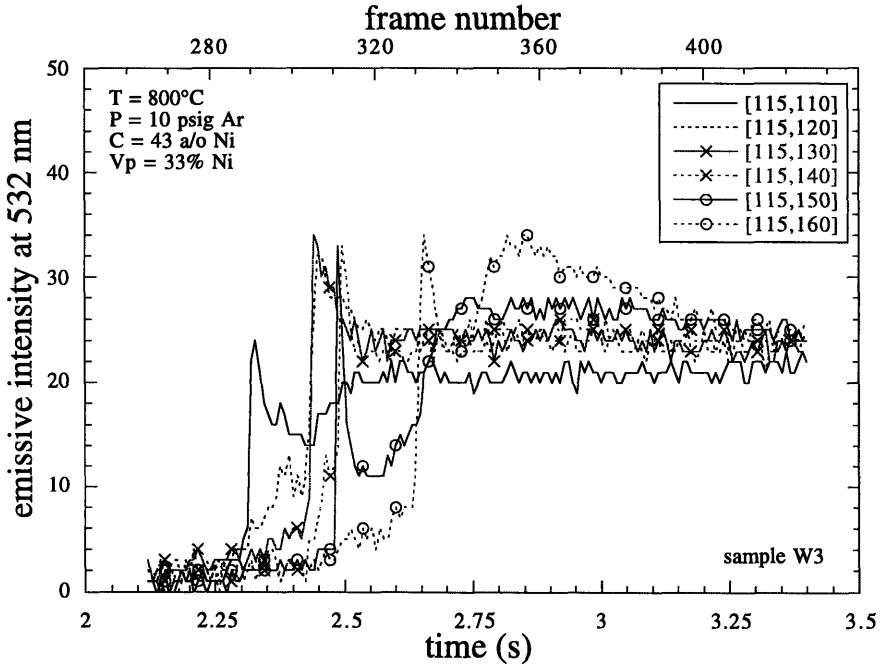

Fig. 5.8b. Emissive intensity for Sample W3, N_{Ni} = 0.43, in the unsteady propagation regime (79 pixels = 1 cm).

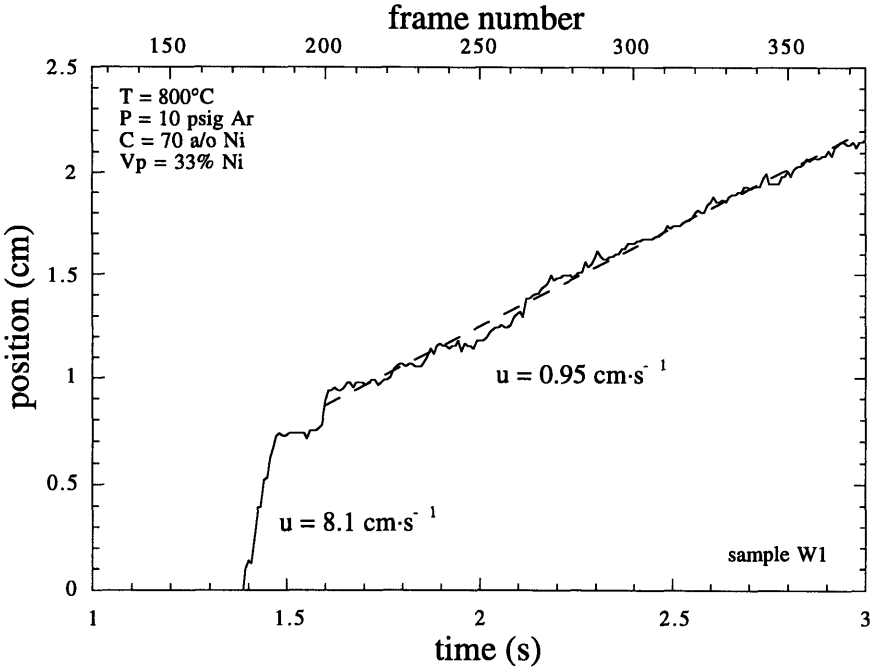

Fig. 5.9. Position versus time curve for Sample W1, N_{Ni} = 0.70.

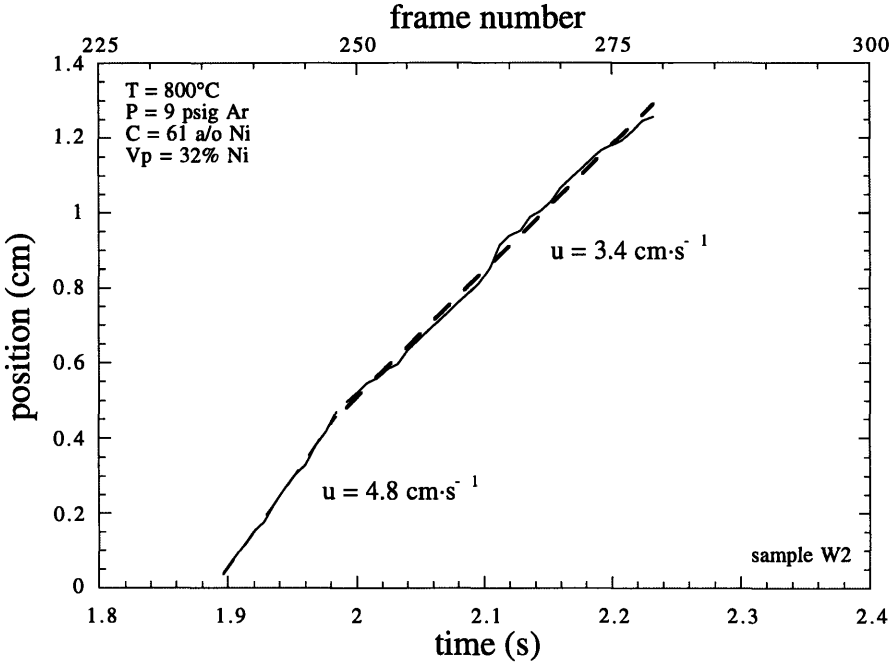

Fig. 5.10. Position versus time curve for Sample W2, N_{Ni} = 0.61.

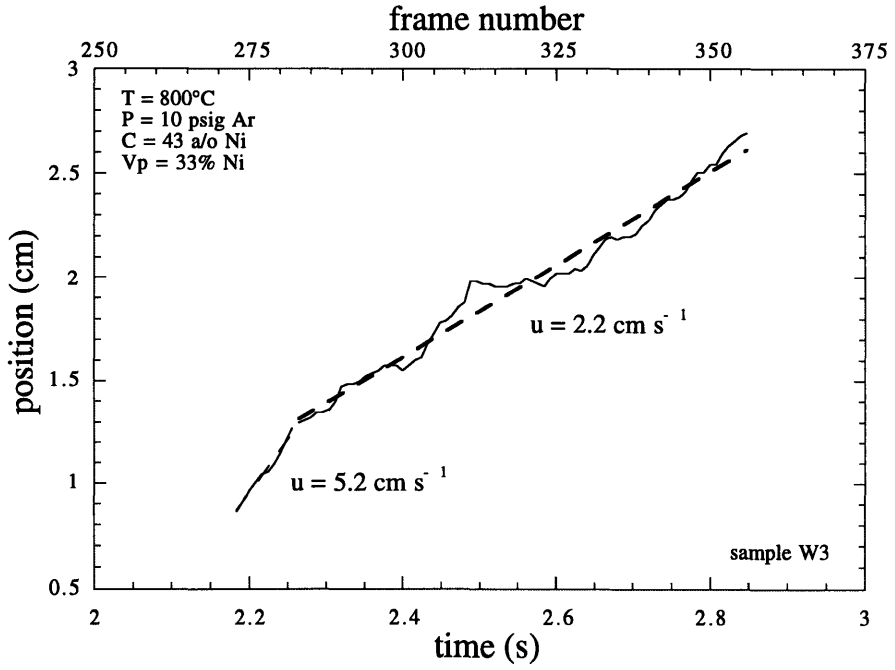

Fig. 5.11. Position versus time curve for Sample W3, N_{Ni} = 0.43.

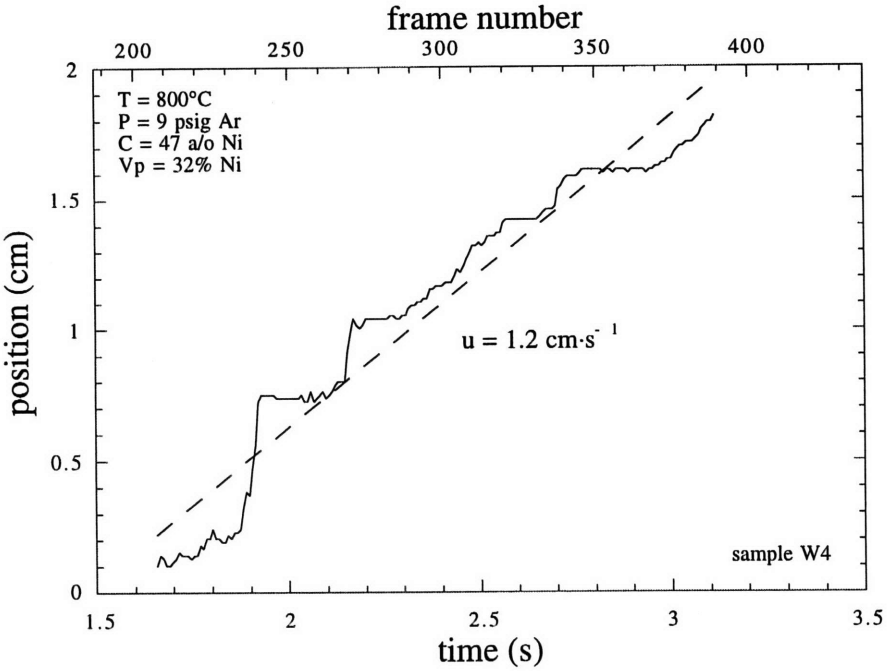

Fig. 5.12. Position versus time curve for Sample W4, $N_{Ni} = 0.47$.

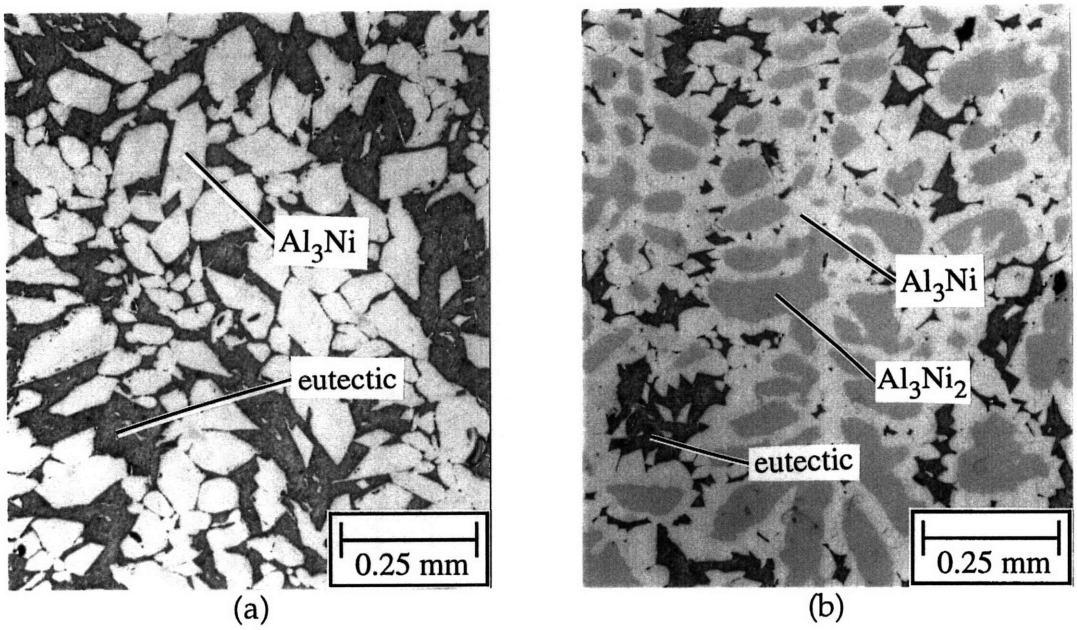

Fig. 5.13. Optical micrographs of the aluminum-rich zone from Sample E60 showing: (a) the faceted Al_3Ni phase surrounded by eutectic material near the top of the aluminum-rich zone; and (b) the increased nickel content in the aluminum-rich zone near the interface with NiAl: dendrites with a core of dark uniform Al_3Ni_2 surrounded by lighter Al_3Ni with small amounts of eutectic material.

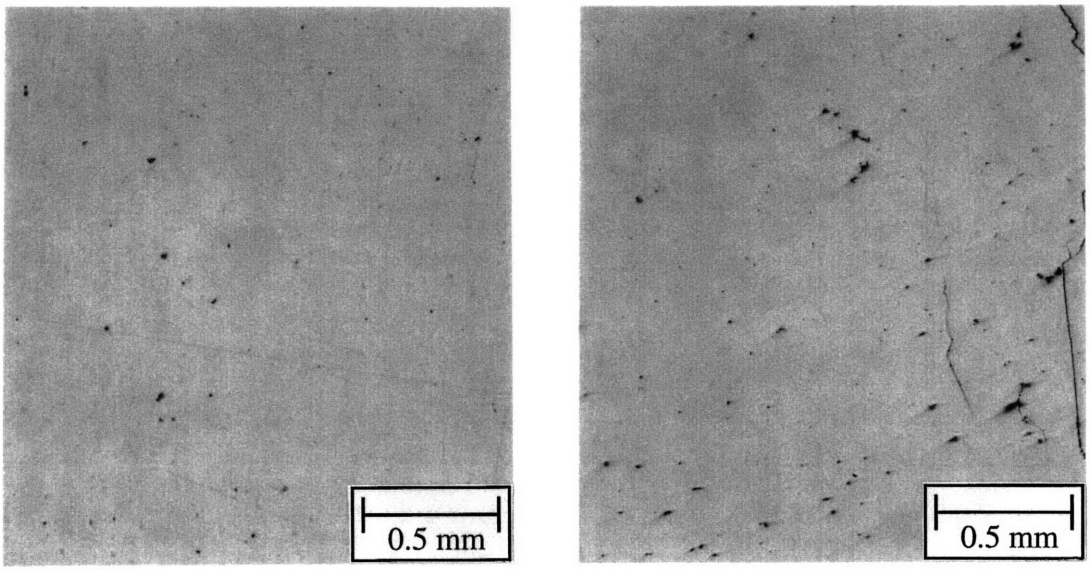

(a) (b)

Fig. 5.14. Optical micrographs of homogeneous NiAl in (a) Sample E60 (Al-rich sample) and (b) Sample E53 ("free wire" sample).

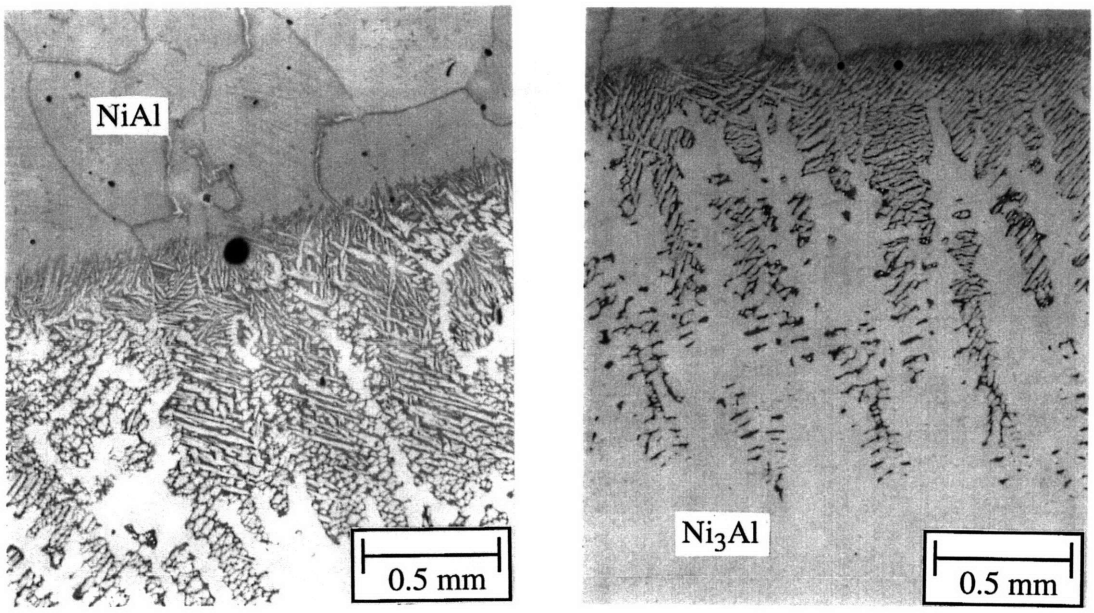

(a) (b)

Fig. 5.15. Optical micrographs (etched) of the boundary between NiAl and Ni_3Al in Sample E51. Grain boundaries are evident in the upper NiAl region (a), while the lower Ni_3Al region is relatively featureless (b).

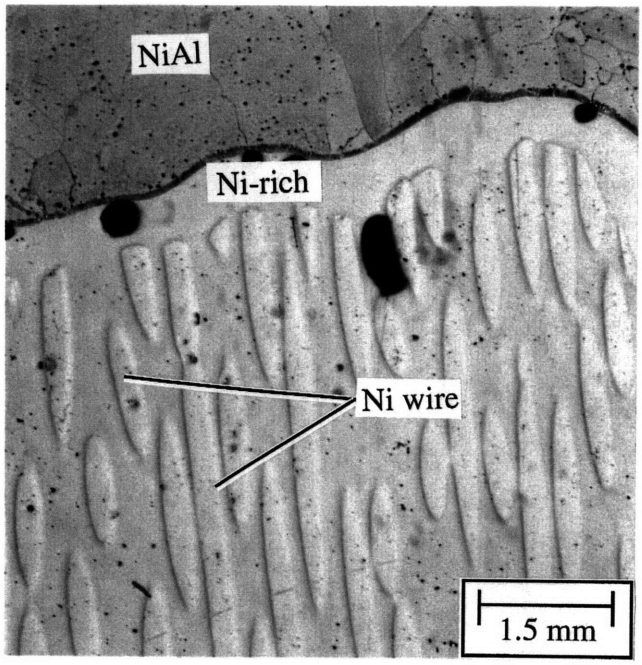

Fig. 5.16. Optical micrograph (etched) of boundary between the darker NiAl and the lighter nickel-rich phases in Sample E47 ("free wire" sample), showing nickel wires infiltrated with nickel-rich material.

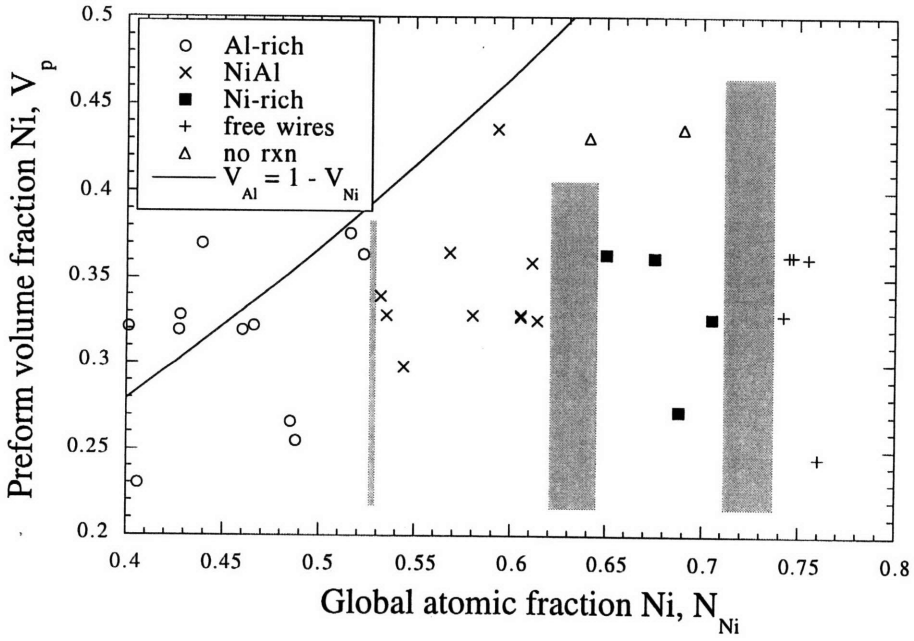

Fig. 5.17. Processing map for all experiments conducted using nickel wire preforms.

6. Discussion

6.1. Rapid local reaction

One can consider two limiting cases in reactive infiltration, depending on the rate of local reaction relative to the rate of infiltration. One limiting case is when the rate of local reaction is rapid in relation to the rate of local flow, such that everywhere within the porous preform and at every instant during infiltration, local equilibrium is rapidly established over a volume element the size of preform pores. The second limiting case is when infiltration is sufficiently rapid that there is, essentially, no local reaction. In this latter case, all chemical interaction between the solid and an essentially stagnant liquid takes place after infiltration.

In this section the first limit is considered, in which local reaction rates are very rapid. Since the permeability varies as the square of the average pore radius, eqn. (2.10), whereas capillary forces vary as the inverse of the average pore radius, the smaller the pore size, the lower the rate of infiltration. Furthermore, local reaction rates increase as the particle size decreases. Therefore, it is clear that the rapid reaction limit is pertinent, when considering preforms of small particles.

In the rapid reaction limit, the liquid composition must be determined by local equilibrium with the solid wherever it is present. Two assumptions can be made with regard to the solid composition: (i) if solid state diffusion is sufficiently rapid to equalize concentrations within the solid, or if temperature changes cause remelting and reprecipitation of the solid, the solid is homogeneously at the equilibrium composition given by the phase diagram; or alternatively, (ii) it can be assumed that, although the solid is locally at the equilibrium composition near the solid/liquid interface, most of the solid retains the composition it had when it formed, since solid state diffusion is generally sluggish. In either event, the local liquid composition is fixed by the local temperature and the nature of the solid phase present.

The distributions of temperature and phase volume fractions within the preform during infiltration are largely governed by the strongly exothermic reaction between aluminum and nickel. Temperature can, therefore, vary widely: this complicates the problem significantly, because the nature of

phases present can, therefore, also vary from one location to another and must be predicted as well.

Governing equations within each two-phase region are:

(i) Continuity: $$\nabla \mathbf{v_o} = 0 \tag{6.1}$$

where v_o is the superficial velocity;

(ii) Darcy's law: $$\mathbf{v_o} = -\frac{K}{\mu}\nabla P \tag{6.2}$$

where P is pressure, μ is the melt viscosity, and K is the permeability of the porous preform, section 2.4.2;

(iii) Conservation of heat: $$\nabla(\mathbf{k}\nabla T) = \rho c \mathbf{v_o}\nabla T + \frac{\partial H}{\partial t} \tag{6.3}$$

where **k** is the thermal conductivity tensor of the infiltrated preform, ρ is the density of the molten material, c is the heat capacity of the flowing infiltrate, and H is the volumetric enthalpy of the combination of phases locally present at temperature T;

(iv) Solute conservation: $$\frac{\partial \overline{C}}{\partial t} = -v_o \nabla C_L \tag{6.4}$$

where C_L is the solute concentration in the liquid, written under the (generally legitimate) assumption that mass transport by diffusion is sluggish in relation to convective mass transport across macroscopic distances. The average local concentration $\overline{C}$ is defined as:

$$\overline{C} = C_s V_s + C_L (1-V_s) \tag{6.5}$$

where C_s is the solute concentration in the solid and V_s is the volume fraction solid.

When these equations are applied to unidirectional infiltration along the positive x-direction, from the preform entrance at x = 0, the initial and

boundary conditions are as follows, for a system equivalent to the experiments described herein:

(i) at t = 0, the preform is at uniform initial temperature T_0 and remains uninfiltrated;

(ii) at x = 0, for all t > 0, the applied pressure has a given value P_0, and the temperature is either fixed, or is such that it tends toward a constant value at negative infinity (corresponding to a large bath of infiltrate);

(iii) at a well-defined infiltration front, located at x = L, the pressure has a well-defined value, governed at least in part by capillary forces (assuming "slug flow," *i.e.*, that the infiltration front is planar); and

(iv) at positive infinity, the temperature tends towards T_0, or some other temperature, as in Ref. [57, 58] for non-isothermal infiltration experiments.

As for the analogous problem of infiltration in a non-reacting system [65], all previous equations can be transformed under these assumptions by using the Boltzmann transformation, whereby time t and distance x are combined within a single variable χ defined as:

$$\chi = \frac{x}{L} = \frac{x}{\Psi\sqrt{t}} \tag{6.6}$$

where Ψ is defined such that the total infiltrated length L equals $\Psi\sqrt{t}$. All partial derivatives with respect to x and t can, therefore, be transformed into ordinary derivatives of χ in all equations above. Since all initial and boundary conditions are also compatible with this change of variable, the problem can be solved entirely in terms of the single variable χ, although, as indicated above, the problem still remains complex.

Therefore, as infiltration progresses, the infiltrated portion of the preform spreads self-similarly. All local variables, including temperature, fraction solid, nature of phases present and their composition, remain constant at each given fractional length χ.

At the infiltration front, in particular, the temperature and the liquid composition are therefore constant. This can only occur if one of the two following situations is obtained.

The liquid phase at the infiltration front is chemically stable when in contact with pure nickel. If it is assumed that there is insufficient time for significant aluminum diffusion into the nickel preform elements during infiltration, the temperature and the liquid composition at the infiltration front must therefore lie along the liquidus line which extends from pure nickel at 1728K to nickel-rich eutectic at 1658K.

Alternatively, as the liquid comes into contact with pure nickel preform elements, the liquid phase at the infiltration front can react instantaneously to form a different solid phase. Since the liquid composition is unchanged, this solid, formed by reaction of the liquid with pure nickel, must be richer in nickel than the liquid. Its concentration is then dictated by the following solute conservation equation:

$$V_s C_s = V_o C_{Ni} + (V_s - V_o) C_L \tag{6.7}$$

where C_{Ni} is the concentration of pure nickel, V_o is the initial volume fraction nickel present in the preform, and C_L, C_s and V_s are the liquid concentration, the solid concentration, and the volume fraction solid behind the infiltration front, respectively. Rewriting eqn. (6.7) as:

$$\frac{V_s}{V_o} = \frac{C_{Ni} - C_L}{C_s - C_L} \tag{6.8}$$

and assuming equilibrium compositions from the phase diagram, this equation implies that the volume fraction of the new solid phase formed exceeds that of the original preform, since no solid Al-Ni intermetallic phase is such that V_s could be lower than about three to four times V_o.

With preforms employed in this work, therefore, when infiltration occurs, the microstructure of the region near the infiltration front must consist of the original nickel spheres surrounded by a solidified liquid whose composition is greater than 0.75 atomic fraction nickel. Also, in the limit of very rapid local reaction, the temperature at the infiltration front is somewhat below the melting point of pure nickel.

Since pure aluminum above its melting point is at local equilibrium with no solid phase, it must alter its composition in a step-wise fashion at the moment it comes into contact with solid within the preform. This is

accomplished by reaction between the infiltrating aluminum and the first solid phase it encounters, such that the liquid increases its nickel content by dissolving nickel-rich solid as it flows over the solid, along a sharp dissolution front. This dissolution front is expected to be unstable, the driving force for instability being the far lower resistance to flow of the liquid on the upstream side of the front compared to the downstream semi-solid infiltrated preform region. Indeed, if a protrusion into the semi-solid region forms along this dissolution front, liquid flows faster at the protrusion, since flow within the pure aluminum is faster for a given pressure gradient than within the porous medium immediately downstream of the dissolution front. This, in turn, causes accelerated dissolution, and the protrusion grows further, thus destabilizing the dissolution front.

The stability of similar planar dissolution fronts propagating at a constant velocity was analyzed by Chadam *et al.*, but without accounting for heat transfer, unfortunately making this analysis non-applicable to the present problem [66, 67, 68]. Heat evolution at the dissolution front is likely to further destabilize the front because of the instability in dissolution, as described in section 3.4. The problem of a remelting front forming when cold inert preforms are infiltrated by superheated metal was analyzed for a pure infiltrate and a front propagating at steady state in Ref. [69].

Assuming rapid local reaction kinetics, the liquid phase cannot coexist with more than one solid phase between the dissolution front at the preform entrance and the infiltration front. It is therefore expected that at any instant t during infiltration, a series of regions are encountered, in which the nature of the solid phase present changes abruptly from one phase to another as the temperature varies across transformation temperatures, such as the Al_3Ni_2 peritectic, Fig. 2.1. As for dissolution of solid in contact with incoming liquid, solid phase changes occur along well-defined boundaries. Interfaces separating bands of varying phase structure are therefore expected to appear in the final infiltrated structure, perhaps somewhat blurred by interdiffusion during the time elapsed between cessation of infiltration and full solidification of the structure.

The structure of infiltrated preforms produced using nickel powders indeed shows the features described above:

(i) there are various regions of relatively constant structure separated by well-defined interfaces;

(ii) there is a dissolution front behind which the aluminum was visibly fully liquid (the composition was hyper-eutectic);
(iii) there are clear signs of instability in this dissolution front, as shown by veins of aluminum-rich liquid that penetrate the length of the preform, Fig. 5.1, and as would be expected, this instability affects the planarity of all other downstream phase bands; and
(iv) finally, there is a region in which the nickel spheres have clearly retained their identity after being infiltrated with a highly nickel-rich phase.

Conclusions from both experiment and analysis, show that when infiltration occurs concomitant with significant reaction but without choking of flow (by formation of fully solid material along the infiltration path, as observed in several other studies [40, 47, 48]), the resulting structure features banded regions of varying composition, separated by relatively well-defined interfaces which propagate, behind the infiltration front and in the same general direction as the front, in an unstable fashion. Similar banded regions varying in concentration from essentially pure aluminum to essentially pure nickel were observed by Dunand *et al.* in samples prepared by the same technique [57, 58]. These features are distributed erratically because of instability in the first dissolution front, and result in infiltrated multi-phase intermetallics of little practical interest. For this reason, neither process analysis nor experimentation were pursued further for the rapid reaction limit; rather, emphasis was placed on an exploitation of the other limiting case, namely rapid infiltration, and slow, or more appropriately, delayed reaction.

6.2. Rapid infiltration/slow reaction

6.2.1. Infiltration

Preforms of parallel bundles of coarse nickel wire were prepared to study the rapid infiltration/slow reaction limit of RIP. Aligned wire preforms provided a straight, uniform melt flow path because of the unidirectional nature of the preforms, and aided manufacturing preforms whose global composition after infiltration was located within the single phase field of NiAl. Table 6.1 compares the permeabilities of preforms prepared from the

Table 6.1. Blake-Kozeny permeability of several types of nickel preforms

diameter (μm)	density ($g \cdot cm^{-3}$)	volume fraction	permeability ($cm^2 \times 10^7$)
powders			
150	4.1	0.46	11
wires			
1000	3.1	0.35	3340
380	3.1	0.35	482

powders used above with those of preforms prepared using wires 380 μm or 1 mm in diameter. These values are estimated using the Blake-Kozeny permeability, eqn. (2.10). Compared to powder preforms (prepared from 150 μm diameter powder packed a volume fraction of 0.46), wire preforms used in this work have permeabilities about three orders of magnitude greater. From these significant differences in permeability, it can inferred that powder preforms and wire preforms behave quite differently during infiltration; powders featured significant reaction during infiltration, as concluded in the previous section, whereas wires infiltrated rapidly with subsequent reaction, to be discussed in detail below.

The average velocity of infiltration was measured to be approximately 40 $cm \cdot s^{-1}$ from the video record, Table 5.1. Darcy's Law is generally accepted for Reynolds numbers

$$Re = \frac{D_w \rho_m v_o}{\mu V_p} \tag{6.9}$$

less than approximately unity, where D_w is the nickel wire diameter, ρ_m is the density of the molten aluminum, and the other parameters are as defined in section 2.4.2. Assuming the thermophysical properties for pure aluminum listed in Table 6.2, and using the experimentally determined infiltration velocity 40 $cm \cdot s^{-1}$ for a preform with a volume fraction of 0.33, the Reynolds number is equal to 750; therefore, the fluid flow is not dominated by viscous friction within the preforms and Darcy's Law is not applicable [65].

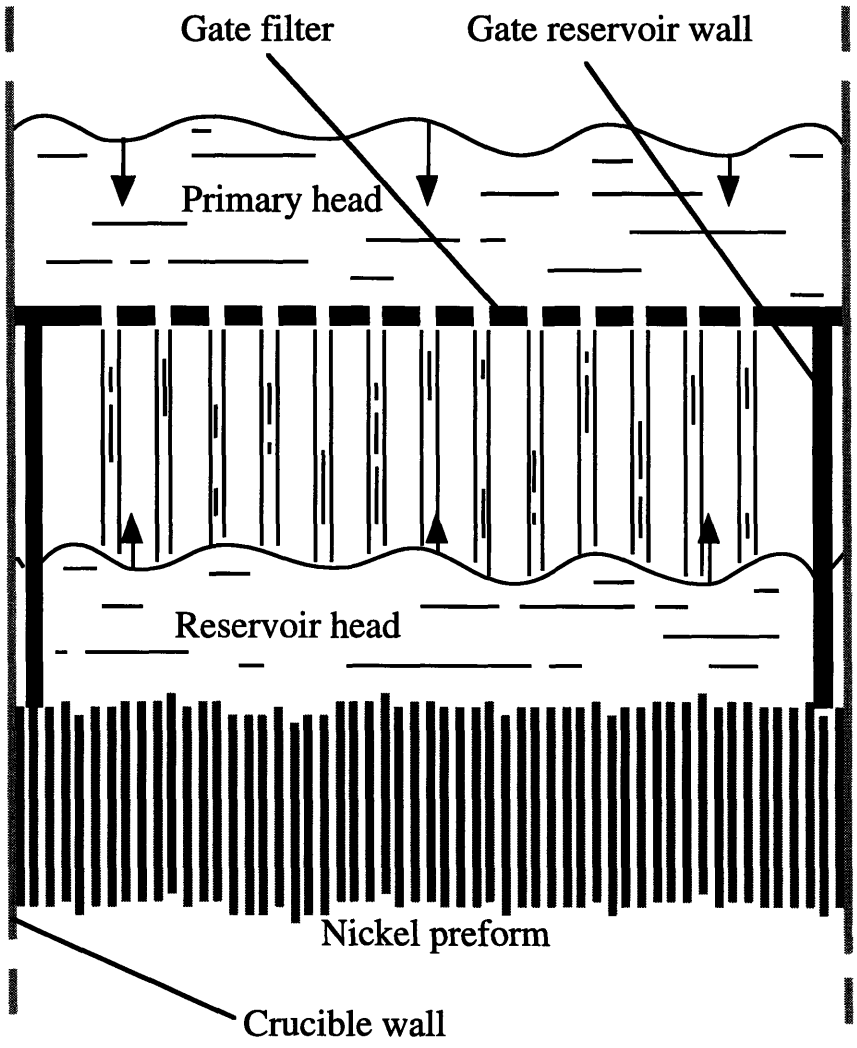

Fig. 6.1. Schematic of the effects of the gate system on initial flow of molten aluminum. The entire applied pressure is dropped across the gate filter, resulting in capillary driven infiltration until the reservoir head is pressurized.

Table 6.2. Thermophysical properties of pure liquid aluminum [70].

temperature (°C)	700	800
density ($g \cdot cm^{-3}$)	2.374	2.346
viscosity (mPa·s)	1.147	0.948
surface tension ($N \cdot m^{-1}$)	0.900	0.865

The permeability of the gate filter was estimated, and found to be significantly larger than the permeability of the preform; however, as long as the reservoir above the preform is not completely filled, liquid in contact with the preform is not pressurized, Fig. 6.1. Initially, therefore, aluminum penetrates the preform solely under the action of capillary forces, until either (i) the height of the fluid in the reservoir head reaches the filter and merges with the primary head, or (ii) the liquid above the filter runs out, at which point the reservoir head is pressurized.

Since aluminum wets nickel, when flow is driven by capillary forces, the metal will flow first into narrow channels between close-packed wires, while large channels remain uninfiltrated. Under the influence of a large external force, however, the microscopic flow path is shifted into larger pores, so as to minimize viscous friction. Capillarity-driven, partially-saturated flow observed in the early stages of infiltration should therefore give way to more fully-saturated flow when the fluid above the preform is pressurized.

This was clearly observed in experiments where the infiltration event was recorded as shown in Fig. 5.2. Initially, the molten aluminum penetrated the preform along narrow internal channels, and only subsequently filled the larger gap between preform and crucible wall when the molten aluminum was pressurized.

If the total volume of aluminum is only slightly less than the total volume of pore space present within the preform, a region of fully-saturated aluminum will exist at the bottom of the preform, while the top of the preform will contain the irreducible volume fraction of aluminum V_{Al}^{ir} defined in Section 2.4.2. The "filter" experiments, where only a small amount of aluminum compared to the initial charge de-wetted the nickel after passing through the entire length of the preform, shows evidence of the irreducible saturation in this system. Such irreducible wetting fluid saturations are commonly observed in the flow of immiscible fluids through porous media [45, 46], and can be due both to chemical hysteresis in wetting, caused by chemical alteration in the solid/liquid interface, and to hysteresis resulting from the geometry of pores within the preform. The average V_{Al}^{ir} was estimated at 0.38, by measuring the height of the fully saturated region and assuming that the remainder of the preform had a uniform distribution of molten aluminum, using images from Sample W11 where this phenomenon was clearly observed. An image of the discontinuous saturation in Sample

W11 is not shown here, because the images were only archived in analog format and re-digitized images have poor contrast.

If the volume of aluminum is less than the volume required to uniformly distribute aluminum in the preform to the irreducible volume fraction V_{Al}^{ir}, infiltration must cease before reaching the bottom of the preform. In the free wire samples, infiltration clearly stopped before the entire preform length was infiltrated, leaving uninfiltrated wires at the bottom, which clearly supports this conclusion. The horizontal interface between the free wire region and the homogenous intermetallic region is also an indication that, at least with the gate system used in the present experiments, initial capillary flow of the infiltrate takes place relatively uniformly across the preform cross-section; this observation is also suggested by video images, Fig. 5.2.

To summarize, infiltration of the preforms does not take place initially in the slug-flow mode; rather, flow is strongly influenced, initially at least, by capillary forces, which tend to distribute the melt in regions of high-nickel content, that is, in regions with the narrowest channels. The effective permeability is then far lower (since the liquid is wetting) than the average preform permeability calculated above [46]. This unsaturated capillary flow is followed by pressurized flow when enough liquid aluminum exists at the preform entrance.

It was also observed in the experiments that initial flow of the melt into the preform is accompanied by relatively little chemical interaction between aluminum melt andthe nickel wire. This was shown by the "filtration" experiment, which showed that aluminum flushed through a preform has dissolved less than 3% nickel. This conclusion is reinforced by the video record of infiltration, which shows no significant sample heating during visible flow of the infiltrate. Rather, the preform was infiltrated, then slowly self-heated after completion of infiltration, as manifest by uniform glowing of the entire infiltrated region in the infiltration video record until the video sensing elements were saturated by the glow.

6.2.2. Reaction

Although it was observed that no significant reaction occurred during infiltration, the system was found to self-heat gradually for 2-3 seconds

thereafter, Table 5.1. This incubation stage is believed to be governed by diffusion in the aluminum-rich liquid.

This assumption can be tested by comparing the average pore radius r_p in the preform with the diffusion distance:

$$x = \sqrt{D\,t} \tag{6.10}$$

where t is the observed incubation time, about 2 s, and D is the solute diffusion coefficient for nickel in liquid aluminum, equal to 4×10^{-5} $cm^2 \cdot s^{-1}$ at 700°C [71]. This former quantity can be estimated by assuming that the cross-section of each wire is isolated in equivalent squares of $2r_p + 2r_w$ on a side, such that the volume fraction in the preform is a ratio of the cross-sectional area of the wire A_{wire} to the area of the associated square A_{square}:

$$V_{Ni} = \frac{A_{wire}}{A_{square}} = \frac{\pi (r_w)^2}{(2r_w + 2r_p)^2} \tag{6.11}$$

The estimated values for x and r_p are both near 100 μm. It is therefore reasonable to attribute the initial uniform self-heating stage observed to exothermic dissolution of the nickel wires into the melt, at a rate limited by diffusion within the liquid. Furthermore, since diffusion through a thickening solid reaction layer would be far slower, there must be no limitation on the rate of diffusion in the liquid by solid intermetallic layers separating the liquid from the solid nickel wires during the incubation stage. Rather, solid intermetallic layers that may have formed must melt back during dissolution without limiting the rate of diffusion into the liquid phase.

This interpretation is consistent with thermodynamic calculations presented in Section 3.4, which show that there is significant heating associated with mixing nickel and liquid aluminum. Heating increases the equilibrium nickel content of the liquid, in turn causing accelerated dissolution of any solid in contact with the liquid. In other words, solid intermetallic layers do not grow as in diffusion couples, but they recede in contact with the dissolving nickel surface. Microscopic observations by Aleksandrov *et al.* using TEM of small samples of molten aluminum in contact with nickel support this conclusion [33].

The incubation stage ends with the initiation of a self-propagating reaction front, similar to fronts observed in SHS-processed powder compacts. In all samples but one, initiation of the reaction front was observed at the preform entrance (*i.e.*, at the preform top), followed by propagation of the combustion front downwards through the sample, Figs. 5.4, 5.5, and 5.6, although no particular device was used to trigger combustion front propagation. Such spontaneous ignition and propagation of a combustion front has also been observed elsewhere in Al-Ni powder compacts of nominally 50 atomic percent nickel processed in the "explosion combustion" mode (*i.e.*, by global sample heating) [23] .

Ignition of the reaction front is likely to be caused by local melting of nickel and the corresponding enthalpy release as the melted nickel mixes rapidly with aluminum-rich liquid. This is seen quantitatively in Fig. 3.4: the enthalpy change upon mixing solid nickel at its melting point, and nickel-saturated aluminum in an equimolar Al-Ni system, is manifested as the discontinuous reduction in enthalpy at 1728K. Melting of nickel within the infiltrated samples is therefore a locally unstable process, because it is accompanied and driven by significant net release of energy. High-speed images indeed show ignition of the combustion front concurrent with formation of a fully molten phase that slumps and leaves no evidence of precursor wires in that region, Fig. 5.3, *i.e.*, initiation and propagation of the combustion front depends on local melting of the nickel preform. Anselmi-Tamburini and Munir also found that the ignition of reaction fronts in SHS of laminated foils was associated with melting of the nickel metal [8, 9].

The simplest explanation for the location of combustion front initiation in this study is that a temperature gradient was present across the length of the sample, such that the top portion of the infiltrated preform was slightly hotter than the rest. Such a temperature gradient could naturally result from convection in the furnace atmosphere. A second cause could be limited density-driven segregation of aluminum-rich liquid to the top of the infiltrated preform, causing the total energy release per unit volume of dissolved nickel to be somewhat higher near the top of the sample. Segregation was, in fact, observed in the final sample macrostructures.

As the combustion front propagates, a zone of liquid Al-Ni alloy was created in its wake. Downward motion of the reacted liquid towards the front was driven by the collapse of unfilled pores which were present within the

infiltrated preform due to partial-saturation of the preform, and by the large volume decrease which accompany formation of the intermetallic phases. It appears that the increased rate of heat loss through the transparent quartz crucible in the video samples due to radiation caused a skin of metal to solidify on the surface of the crucible within the reacted (and therefore liquid) region. With the addition of the large volume change, it seems, this solidification contributed to the formation of the large voids or bubbles that were observed during combustion, Fig. 5.6. Bubbles of this size were never observed in samples produced in the high-pressure infiltration apparatus, where samples do not lose heat by radiation.

Moreover, digital video showed rapid, modest variations in brightness in the reacted liquid for all of the experiments; these are most likely indications of temperature or compositional gradients, concurrent with fluid flow due to natural convection. Indeed, these variations look like a plume of smoke within the sample. However, exclusively in nickel-rich samples, localized, intense bright spots were seen propagating upwards, Fig. 5.4b. These spots were presumably due to an inhomogeneous distribution of liquid in the preform before ignition. Indeed, the maximum combustion temperature T_c occurs at stoichiometric NiAl, 50 atomic percent nickel; regions within the sample that have a stoichiometry closer to 50 atomic percent nickel release more heat and generate the "hot" spots visible on the recorded images. Natural convection will, of course, cause motion of fluid in the presence of large temperature gradients. The observation that no hot spots developed within the aluminum-rich samples also supports this interpretation, since the preform in the aluminum-rich sample was nominally saturated with aluminum and therefore could not have a significantly inhomogeneous distribution of liquid.

This experimental evidence suggests the possibility of continued phase changes behind the combustion front and implies that the combustion front temperature, T_c, may have differed from T_{ad}, the calculated adiabatic temperature for full reaction, or in other words that there was afterburning behind the reaction front. However, in the present experiments, it is believed that this phenomenon should not occur because: (i) afterburning is created when there is a strong reduction in reaction rate with increasing extent of reaction [72], but with no thickening barrier to reaction in a fully liquid reaction, such a drastic reduction in local reaction kinetics is not expected; (ii)

convection in the liquid reaction product can rapidly remove temperature gradients within the region extending behind the reaction front; and (iii) temperature profile measurements of Maslov *et al.* [30] for combustion synthesis of NiAl with T_{ad} above the NiAl melting point show temperature profiles featuring a sharp increase before the reaction front, and no temperature gradient thereafter, typical of a reaction front featuring no afterburning [4].

It therefore seems justified to take $T_c = T_{ad}$, at least as a first approximation when applying eqns. (2.1) and (2.3) for the combustion front velocity. The only data found in the literature for combustion velocities of equiatomic aluminum and nickel with initial temperatures sufficiently high to yield fully liquid NiAl are the experiments of Maslov *et al.* [30].

Given the lack of consistency in activation energies collected from experimental data in the literature, rather than deriving values for constants in expressions for u, the expected front velocity is estimated on the basis of the data of Maslov *et al.* and differences in process parameters between the two studies. In the video experiments, $T_o = 1073$ K and $T_{ad} = T_c = 2210$ K. Extrapolating slightly the data of Maslov *et al.* from $T_c = 2100$ K to this temperature yields $u = 20$ cm·s^{-1}, Fig. 2.2. According to eqn. (2.3), there are three factors which should cause differences between front velocities in the samples presented here compared to those of Maslov *et al.*: (i) reactant particle size δ, (ii) thermal diffusivity α, and (iii) the difference between the combustion temperature and the initial reactant temperature, $T_c - T_o$.

In the powder compacts of Maslov *et al.*, the nickel particle size was reported to be "less than 45 μm". The average nickel particle size is assumed to be around 40 μm in their experiments, and to determine the characteristic diffusion distance because the aluminum particle sizes were significantly smaller (1 to 5 μm). With an initial wire diameter of 380 μm in the video experiments, the influence of an increased diffusion distance δ should cause a decrease by a factor of 10 in the propagation velocity u.

In the present infiltrated wire preforms, the value of the thermal diffusivity α was that of the dense reactant mixture, whereas in the powder experiments of Maslov *et al.*, the presence of 40% porosity in the reactant mixture lowered α compared to a fully dense continuous system. In the porous mixture both the thermal conductivity and the heat capacity are assumed here to be lowered by a factor near 2; therefore, particle size should

exert a more significant influence than porosity (in the preforms of Naiborodenko and Itin, the decrease in u was associated with the onset of unstable front propagation [27]).

The final difference in experimental conditions is that the present samples were heated by a relatively slow reaction before propagation of the combustion front, whereas in the experiments of Maslov *et al.*, samples for which $T_c \approx 2100K$ were only preheated to $T_o \approx 740$ K. The factor $T_c - T_o$, which appears in eqns. (2.1) and (2.3), should, therefore, be smaller in the present experiments to account for the same final adiabatic temperature T_c. This effect would cause a modest increase by a factor of $(T_c - T_o)^{-1/2}$ in the front propagation rate compared with that found by Maslov *et al.* for a given T_c.

Combustion front propagation velocities, in the present case, therefore, are expected to be somewhat greater than one tenth the velocity derived from the experiments of Maslov *et al.*, *i.e.*, to exceed 2 $cm \cdot s^{-1}$ by a quantity that depends on the modified thermodynamics of this system. This prediction agrees rather well with recorded velocities, Table 5.1.

Variability in the theoretical relationship between the front ignition event (caused by locally enhanced reaction rate) and the overall sample temperature T_o (which is governed by the progress of the slow-diffusive heating during incubation) provides at least one explanation for the difference in the velocities recorded in this study. Other factors accounting for the variance between the experiments performed here and those of Maslov *et al.*, might be: (i) temperature gradients within the samples in the present study; and (ii) the stoichiometry of samples in the present study which varied and was generally closer to $Ni_{0.6}Al_{0.4}$, compared to the equiatomic concentration of powder mixtures explored by Maslov *et al.* and other researchers. The greater initial front propagation velocity recorded with most samples could represent a transition from initial transient propagation to true steady state propagation, or could be the result of a change in convection patterns within the reacted zone.

Maslov *et al.* also showed that as T_c increases, the velocity of the combustion front u increases, therefore, the largest combustion velocities are expected at compositions near stoichiometric NiAl. This was not observed in the present experiments, for which no clear correlation between process parameters and u could be found, possibly due to mass convection and heat losses. It is noted, however, that global composition and not initial

temperature was varied in the present experiments, which are therefore qualitatively different from those of Maslov *et al.*

Theoretical criteria for combustion front stability depend strongly on the value of the activation energy E, the uncertainty of which precludes using stability criteria directly to interpret the present data. Maslov *et al.* report no observation of front instability in their powder-based samples, while Naiborodenko and Itin [27] found that their samples either displayed unstable front propagation, or were at the threshold of stability. Since the combustion temperature T_c is higher for all the present experiments compared with other studies, and since $(T_c - T_o)$ is lower (or equivalently ΔH is lower), all fronts should be stable in the present experiments, based on existing theory. This differs somewhat from the present observations: although stable front propagation was observed initially, after a finite distance the combustion fronts became unstable.

On the other hand, observations of instability in the present samples could be taken to agree with those of Li and Sekhar [23, 24] who found that for nickel powder particles above 8 μm in diameter, banded structures typical of pulsed-front propagation resulted, although predicted adiabatic combustion temperatures were such that the product was mostly molten NiAl at its melting point. Such a dependence of front stability on particle size is not, however, predicted by theory.

The onset of unsteady propagation in the present samples may also be influenced by radiative and conductive heat losses to the surroundings, as well as convection in the reacted liquid portion of the samples. In particular, Sample W2, which experienced intense convection that developed at the same time and in a region quite near the position in the sample where the combustion front became unstable, Figs. 5.4 and 5.7, provides an indication of a correlation between convection in the reacted zone and stability of front propagation.

Finally, there is a possibility that the combustion was not characterized by a single front that ignited at the preform entrance in the high-pressure apparatus. There is no evidence to suggest this is the case, and in fact the macrostructure also seems to be independent of the location where the combustion front ignited; Sample W11 ignited halfway along the length of the sample and featured the same resulting macrostructure as Sample W16, which had nominally the same composition, but ignited at the top. If the

presence of a temperature gradient is a necessary ingredient in localized ignition, this may have been absent in the better controlled thermal environment of the high-pressure system.

6.2.3. Reacted sample macrostructure

The processing map, Fig. 5.17, for the production of nickel-aluminides shows that, as expected, the phases present in the reacted samples vary with global composition: the transition between macrostructures is a function of this single variable for all reacted samples produced in this work from wire preforms.

According to the phase diagram, a uniform sample of NiAl cannot contain more than a global atomic fraction nickel N_{Ni} of 0.60. This agrees approximately with the observed transition between nickel-rich samples and monolithic NiAl samples, Fig. 5.17, which occurs between N_{Ni} 0.61 and 0.65. Furthermore, the estimated irreducible-volume saturation $V_{Al}^{ir} = 0.38$, determined from infiltration data in Section 6.2.1, corresponds to a N_{Ni} of 0.61 in samples filled uniformly to the irreducible saturation. This agrees with the observed transition between monolithic and nickel-rich sample macrostructures. Hence, this transition can be linked to incomplete infiltration of the sample length when the global aluminum content falls below V_{Al}^{ir}. The fact that this transition occurs precisely at the compositional bound of the single-phase NiAl region on the phase diagram is thus presumably a coincidence.

In nickel-rich samples of N_{Ni} greater than about 0.61, the volume of aluminum is thus not sufficient to fill the preform to the irreducible volume saturation V_{Al}^{ir}. If the amount of aluminum is very lean, a significant portion of the preform will remain uninfiltrated. The free wire samples were formed in this manner for N_{Ni} greater than 0.74.

The transition between nickel-rich and free-wire samples can be explained by heat exchange between the lower uninfiltrated portion, and the upper liquid intermetallic formed by reaction of aluminum and nickel. The reacted liquid is above the melting point of nickel; hence it can melt adjoining nickel wires. This suggests that the transition between nickel-rich and free wire samples corresponds to the maximum volume of remaining wires that can be fully melted by the reacted NiAl formed above.

The transition can therefore be predicted by equating the energy required to melt n_{Ni} moles of nickel initially at 973K with the energy release associated with cooling and solidifying n_{NiAl} moles of stoichiometric NiAl liquid, which was initially superheated to 2100K (the approximate adiabatic temperature of stoichiometric NiAl processed at 973K):

$$n_{Ni}\left(\int_{973\,K}^{1728K} Cp_{Ni(s)}\,dT + \Delta_m H_{Ni}\right) = n_{NiAl}\left(\int_{1912K}^{2100K} Cp_{NiAl(l)}\,dT + \Delta_m H_{NiAl}\right) \quad (6.12)$$

The molar ratio of melted nickel to reacted NiAl, n_{Ni}/n_{NiAl}, was calculated to be 1.7, corresponding to $N_{Ni} = 0.73$. This agrees well with the observed transition from Fig. 5.17 between 0.70 and 0.74 atomic fraction nickel. The calculated value assumes that stoichiometric NiAl was formed and that the system was adiabatic, although the composition of the reacted intermetallic is determined by the irreducible saturation; therefore, the thermodynamics are slightly modified from eqn. (6.12) if off-stoichiometric conditions are taken into account. These effects would reduce the critical N_{Ni} until it was nearer the lower bound of 0.70.

Heat exchange between the reacted portion of free-wire samples and uninfiltrated nickel wires can also explain microstructural features observed in these samples. First, it is expected that wires immediately adjoining the reacted NiAl zone will melt back to a certain extent (the maximum value of which is determined by the heat balance above). This, in turn, can cause the infiltration of remaining colder wires with nickel-rich liquid under the influence of gravity and capillarity. A homogeneous intermetallic was indeed observed above free wires in samples with N_{Ni} greater than 0.74, and a horizontal interfacial region of a few millimeters thickness was also noted, consisting of nickel wires in a nickel-rich intermetallic matrix between the uninfiltrated wires and the homogeneous intermetallic (although in one sample, the nickel-rich fluid infiltrated over 1 cm of bare wire preform, Sample E47).

The criterion for the transition between monolithic samples and aluminum-rich samples is more difficult to establish, although it seems obvious that if the volume of aluminum is greater than the total pore space in the preform, an aluminum-rich region must be found above the preform

entrance. The curve in Fig. 5.17 represents the case in which the volume of pore space equals the aluminum volume; data points above the curve can clearly be explained in this way. There are, however, several aluminum-rich samples that had excess pore space in the preform, denoted by the open circles with nickel volume fractions less than the critical values represented by the curve.

It seems that N_{Ni} greater than 0.53 is required to produce samples of monolithic NiAl. The fact that this transition is greater than 0.50 or even the lower compositional bound of the NiAl single-phase field on the phase diagram can result from several phenomena: (i) gas entrapment in the preform due to gas leakage around the reservoir head preventing infiltration of all pores by the melt; (ii) poor wetting of crucible (and potentially certain locations of the preform), also preventing full infiltration; and (iii) gravity-driven flow of aluminum contained in larger infiltrated channels to the top of the samples during reaction. The formation of aluminum-rich regions in samples with volume fractions well below the critical volume fraction, as shown in Fig. 5.17, supports the last explanation, as does the observation of significant convection behind the reaction front within the samples observed in high-speed video. This would imply that all transitions are determined by the pore structure of the preform, and that samples having relatively large pores, which allow aluminum to segregate to the top of the fluid before mixing, tend to promote formation of the aluminum-rich layer.

The unreacted samples in Fig. 5.17 were both video samples, which lost more heat in radiation than samples produced using coated crucibles. It is also possible that the high volume fraction nickel in the preforms may have limited the temperature rise during the incubation stage, due to the thermal ballast of the additional nickel, preventing in turn the ignition of a self-sustaining combustion front.

In the above discussion, it has been assumed that the volume fraction nickel in the preform does not affect V_{Al}^{ir}; this assumption cannot be generalized. As the density of the nickel preform increases, the density of small pores also increases, and V_{Al}^{ir} is expected to increase. Similarly, V_{Al}^{ir} could vary with the infiltration temperature (which affects wetting) or the diameter of the precursor wires (which may affect packing). However, the criteria described above have been shown to be effectively independent of both temperature and preform volume fraction, at least within the resolution of

the collected data and the range of variation of the parameters. The specific effects of wire diameter has not been explored here, other than to show that large wires (1 mm diameter) also can react completely to form monolithic NiAl.

6.3. Other preform morphologies: nickel pieces

The experiments with preforms of nickel pieces have not been discussed above because infiltration is greatly complicated by the non-uniform pore structure in these samples. Further study is required to characterize this geometry, but preliminary experiments, Table 5.5, indicate that the infiltration and reaction sequence is qualitatively (but not quantitatively) similar to that of the nickel wire preforms, since similar macrostructures are obtained.

6.4. Engineering potential

From a practical standpoint, the present study demonstrates that dense, bulk samples of single-phase NiAl can be produced by RIP at temperatures near the melting point of aluminum. The requirements for this are not strict: (i) a nickel preform with large permeability; (ii) pure molten aluminum; and (iii) a method of transporting the aluminum into the preform in less than a second. There is a complex interplay between the infiltration rate, preform morphology and system thermodynamics that has not been fully quantified here, nevertheless the above requirements cause the infiltration of the preform and the reactions to be temporally independent.

Additional requirements are necessary to control the major macrostructure defects, namely porosity and macrosegregation. The porosity results from shrinkage during solidification and can be controlled by forcing directional solidification with thermal sinks. Macrosegregation, as investigated in this work, results in well-defined, macroscopic regions of different phases. This can be controlled using proper stoichiometry or considering a portion of the material sacrificial such as a riser in a casting.

Although the scope of the present study is limited to the production of monolithic NiAl, the driving force for developing RIP is the production of complex refined microstructures, *i.e.*, fine-grained NiAl and composites

including other intermetallic systems. Intermetallics are produced industrially by "conventional" melting/casting techniques and more recently by reactive melting and subsequent casting [73, 74]. The Exo-Melt process, in particular, has shown the utility of reactive melting processes: exothermic melting of Ni_3Al is achieved by first forming the more exothermic NiAl phase that can then melt additional nickel to the desired composition [74], similar to the formation of Ni-rich phases described in this study. This technique has some striking similarities to RIP described here, namely the use of liquid aluminum to infiltrate a porous nickel body; however, the Exo-Melt differs in that the infiltration is not strictly controlled, inductive heat input sustains a melt for a significant amount of time, and the intermetallic is subsequently cast into a separate mold.

Casting processes for high-melting materials such as intermetallics have the disadvantage of requiring a superheated melt at temperatures as high as 2000°C. This, of course, requires significant energy input and greatly reduces the cost and lifetime of molds and crucibles, while at the same time increasing the probability of melt contamination. Unlike casting techniques, reactive infiltration processing does not require special tooling for melting the intermetallic phase, rather it only requires molten aluminum casting technology (in the case of aluminide formation), which is a relatively simple and well-established technology. Although in the present study fully-molten, monolithic NiAl was produced during processing due to the exothermic reactions, the peak temperature and time at temperature during processing can be controlled with the addition of thermal ballast in the form of mold chills and pre-alloying the preform with NiAl for example, or by manipulating the initial preform and melt temperatures independently. Thus, RIP could extent the lifetime of molds and reduce energy costs for the production of monolithic intermetallic phases.

Furthermore, the high-temperatures needed for casting make it difficult to produce refined microstructures and composite materials. For example, pressure infiltration casting of NiAl-Al_2O_3 composites causes recrystallization of the Al_2O_3 and loss of desirable properties in the reinforcement [75]. Thus, in the absence of processes for producing intermetallic-matrix composites (IMCs), reactive powder metallurgy has been developed in recent years as a potential production method for these materials. Reactive powder metallurgical methods have shown some success in the production of IMCs,

but these materials are plagued by porosity and contamination, in addition to severe limitations on the type of microstructures that can be achieved, especially with fibrous reinforcements.

Comparatively, reactive infiltration processing is a promising alternative to reactive powder metallurgy for the production of intermetallics and IMCs, because RIP does not have the disadvantages associated with reactive powder metallurgy, *e.g.*, the use of liquid infiltrate eliminates a major source of oxide particularly in systems with aluminum powders and porosity is eliminated by the forced infiltration of a liquid. In addition and maybe more importantly, RIP can produce microstructures that cannot be achieved with reactive powder metallurgy, such as long fibrous or whisker reinforced materials.

Indeed the strength of RIP is the potential for microstructural control inherent in the process. The morphology and range of secondary phases that can be included in intermetallic phases by this route is exceptional compared to other techniques, and moreover the process has potential for the *in situ* production of secondary phases by additional reaction mechanisms. An example of the types of composite structures that can be produced by this technique can be found in the work of Venkatesh and Dunand, who have produced W-fiber reinforced NiAl [76]. Furthermore, the microstructure of the intermetallic itself can be controlled by manipulating the mold configuration, initial preform and melt temperatures, or pre-alloying the preform and melt (*i.e.*, controlling the thermodynamic processes). This process thus additionally allows for rapid solidification of the intermetallic, which may provide a means for producing fine or complex microstructures such as the lamellar NiAl/Ni_3Al microstructure observed by H. Chen *et al.* [49]. The scope of microstructures that can be generated by reactive infiltration processing of NiAl represents perhaps its greatest advantage, and is one that remains to be fully explored within the framework developed here towards understanding and controlling the physics of reactive infiltration in the Al-Ni system.

7. Conclusions

• Nickel powders with diameters in the 150-180 μm range react rapidly during reactive infiltration processing (RIP), forming irregular banded structures of increasing nickel concentration along the global infiltration direction. Assuming rapid local reaction during infiltration, analysis of the process provides an explanation for the formation of this macrostructure.

• Aligned wire (380 μm) bundles were observed to infiltrate and react independently in time. High-speed digital cameras were used to capture a quantitative digital record of the process characterized by three stages: (i) infiltration; (ii) incubation; and (iii) reaction.

• Infiltration was controlled using a special gate system, resulting in capillarity-driven flow of the melt into the preform during the initial stages of infiltration and subsequent pressurization of the fluid. Thus, the metal penetrates the preform along narrow channels and only subsequently fills larger channels under externally applied pressure. The average infiltration velocity was measured in the 10-100 $cm \cdot s^{-1}$ range. Data indicate that once preforms of the type used in this work are infiltrated, de-wetting can only reduce the local aluminum content within the preform to an irreducible volume fraction of 0.38.

• The incubation stage featured slow self-heating uniformly along the sample length, for 2-3 seconds. This stage is interpreted as exothermic mixing within the aluminum melt as nickel dissolves, at a rate controlled by diffusion in the liquid.

• Full reaction was initiated by spontaneous ignition of a propagating combustion front, generally at the top of the sample, concurrent with melting of the solid nickel precursors. The front velocity was measured from the digitized video record in the range of 1-10 $cm \cdot s^{-1}$. These velocities are in qualitative agreement with the results of Maslov *et al.*, except that steady propagation is not observed for the entire length of the sample. Convection

in the melt, and radiative heat losses are believed to be significant during processing.

• The macrostructure of samples produced using wire preforms varied according to the global composition, but was found to be independent of pressure and preform volume fraction, at least for the preform morphology investigated. All samples featured a bulk monolithic NiAl phase, while the individual macrostructures were characterized by the existence of additional intermetallic phases: aluminum-rich phases above the NiAl, or nickel-rich phases below the NiAl. The transitions between macrostructural regions is explained by the combined influence of capillarity during infiltration, heat evolved during the reaction, and gravity.

• Sound monolithic NiAl was produced from aligned wire preforms. This process also applies to the production of fully-dense, continuously-reinforced intermetallic composites.

• Sound monolithic NiAl was also produced by infiltration of preforms derived from pieces of nickel greater than 3 mm in diameter, and nickel wires 1 mm in diameter.

8. Suggestions for Future Work

This study has shown the potential of reactive infiltration processing (RIP) in the Al-Ni system for the production of intermetallics and their composites. Furthermore, it has, at least qualitatively, elucidated several of the underlying physical phenomena, especially the interplay between the infiltration rate, preform morphology and system thermodynamics; it nevertheless raises more scientific and engineering questions than it answers. As a result, RIP provides a seemingly limitless source of interesting problems, some of which are outlined below.

One major shortcoming in this study (and others) is inadequate knowledge of the temperature profile in the sample during processing. The digital camera is an invaluable tool for such measurements because the high spatial resolution (an array of 256 x 256 pixels) and the simple intensity data (256 levels of gray) recorded during processing provides much more information than a single spot pyrometer. However, the system needs to be calibrated which requires knowledge of the emissivity of the reacting material as a function of not only temperature, but composition and structure.

For the Al-Ni system, the effect of preform morphology, namely the size and shape of the pores, and the existence and role played by the irreducible saturation, are now identified but not fully understood. Thus, the complex interplay between the infiltration rate, preform morphology and system thermodynamics needs to be quantified. This would include studying the effect of pressure as function of pore geometry from very high pressures and small pores to pressures produced by hydrostatic gravity and large pores.

Studies on the thermodynamics, on the other hand, have a large number of potential parameters for investigation, *e.g.*, effect of pre-alloying of the melt, initial temperatures, and mold chills. Modeling of the mass and thermal transport in addition to heat evolution could provide quantitative criterion for ignition and reaction-quenching (*i.e.*, extent of reaction). Furthermore, convection was identified in the digital video, but its extent and role in combustion and macrosegregation is not understood. Simple composite preforms can be used to track convection in reacted samples; for example, a small preform of iron embedded in a large preform of nickel can be reacted and the iron concentration mapped in the resulting product. The

effect of secondary phases on the reactions and convection is also necessary for a complete process understanding.

Not only are the above studies required to further the understanding of the *in situ* reaction processes, but they are also necessary for refining the microstructure of the product materials for engineering applications. This study has not rigorously investigated the microstructures of the product, but rather used the product macrostructures to explain physical phenomena during processing towards the development of a physical framework for understanding RIP. Nevertheless, the success of processing monolithic NiAl by RIP warrants studies of the production of composite microstructures for engineering applications, including other matrix systems such as the Al-Ti system.

9. References

1. L.L. Wang, Z.A. Munir, and Y.M. Maximov: *J. Mater. Sci.*, 1993, vol. 28, pp. 3693-3708.

2. Z.A. Munir and U. Anselmi-Tamburini: *Mater. Sci. Reports*, 1989, vol. 3, pp. 277-365.

3. S.D. Dunmead, Z.A. Munir, J.B. Holt, and D.D. Kingman: *J. Mater. Sci.*, 1991, vol. 26, pp. 2410.

4. A.G. Merzhanov: in *Combustion and Plasma Synthesis of High-Temperature Materials*, Proc. Conf., New York, 1990, Z.A. Munir and J.B. Holt, ed., VCH, pp. 1-53.

5. K.A. Philpot, Z.A. Munir, and J.B. Holt: *J. Mater. Sci.*, 1987, vol. 22, pp. 159-169.

6. C. Nishimura and C.T. Liu: *Acta metall. mater.*, 1993, vol. 41, pp. 113-120.

7. H.P. Li and J.A. Sekhar: *Mater. Sci. Eng.*, 1993, vol. A160, pp. 221-227.

8. U. Anselmi-Tamburini and Z.A. Munir: *J. Appl. Phys.*, 1989, vol. 66, pp. 5039-5045.

9. U. Anselmi-Tamburini and Z.A. Munir: in *Combustion and Plasma Synthesis of High-Temperature Materials*, Proc. Conf., New York, 1990, Z.A. Munir and J.B. Holt, ed., VCH, pp. 100-105.

10. J.C. Rawers and H.E. Maupin: *J. Mater. Sci. Letters*, 1993, vol. 12, pp. 637.

11. D.E. Alman, J.A. Hank, J. A.V. Petty, and J.C. Rawers: *J. Metals*, 1994, vol. 46, pp. 31.

12. E. Ma, C.V. Thompson, and L.A. Clevenger: *J. Appl. Phys.*, 1991, vol. 69, pp. 2211-2218.

13. T.S. Dyer, Z.A. Munir, and V. Ruth: *Scripta metall. mater.*, 1994, vol. 30, pp. 1281-1286.

14. T.S. Dyer and Z.A. Munir: *Metall. Mater. Trans. B*, 1995, vol. 26B, pp. 603-610.

15. D.E. Alman and N.S. Stoloff: *Inter. J. Powder Metall.*, 1991, vol. 27, pp. 29-41.

16. W. Misiolek and R.M. German: *Mater. Sci. Eng.*, 1991, vol. A144, pp. 1-10.

17. N.S. Stoloff and D.E. Alman: *Mater. Sci. Eng.*, 1991, vol. A144, pp. 51-62.

18. K.J. Lee and P. Nash: *J. Phase Equilibria*, 1991, vol. 12, pp. 551-561.

19. D.C. Dunand: *Mater. Manufacturing Processes*, 1995, vol. 10, pp. 373-403.

20. A.G. Merzhanov and B.I. Khaikin: *Prog. Energy Combust. Sci.*, 1988, vol. 14, pp. 1 - 98.

21. S.B. Margolis: *Prog. Energy Combust. Sci.*, 1991, vol. 17, pp. 135-162.

22. Y.S. Naiborodenko and V.I. Itin: *Combustion, Explosives and Shock Waves*, 1975, vol. 11, pp. 626-629.

23. H.P. Li and J.A. Sekhar: *J. Mater. Res.*, 1995, vol. 10, pp. 2471-2480.

24. H.P. Li: *J. Mater. Res.*, 1995, vol. 10, pp. 1379-1386.

25. R. Armstrong and M. Koszykowski: in *Combustion and Plasma Synthesis of High-Temperature Materials*, Proc. Conf., New York, 1990, Z.A. Munir and J.B. Holt, ed., VCH, pp. 88-99.

26. S.B. Margolis: *Metall. Trans. A*, 1992, vol. 23A, pp. 15-22.

27. Y.S. Naiborodenko and V.I. Itin: *Combustion, Explosives and Shock Waves*, 1975, vol. 11, pp. 293-300.

28. Y.S. Naiborodenko, V.I. Itin, B.P. Belozerov, and V.P. Ushakov: *Soviet Physics Journal*, 1973, vol. 16, pp. 1507-1511.

29. Y.S. Naiborodenko, V.I. Itin, A.G. Merzhanov, I.P. Borovinskaya, V.P. Ushakov, and V.P. Maslov: *Soviet Physics Journal*, 1973, vol. 16, pp. 872-873.

30. V.M. Maslov, I.P. Borovinskaya, and A.G. Merzhanov: *Combustion, Explosives and Shock Waves*, 1976, vol. 12, pp. 631-636.

31. L.A. Wenning, J.P. Lebrat, and A. Varma: *J. Mater. Synthesis and Processing*, 1994, vol. 2, pp. 125-132.

32. V.V. Aleksandrov, M.A. Korchagin, B.P. Tolochko, and M.A. Sheromov: *Combustion, Explosion and Shock Waves*, 1984, vol. 19, pp. 430-431.

33. V.V. Aleksandrov and M.A. Korchagin: *Combustion, Explosion and Shock Waves*, 1987, vol. 23, pp. 557-564.

34. V.V. Boldyrev, V.V. Aleksandrov, M.A. Korchagin, and B.P. Tolochko: *Dokl. AN SSSR*, 1981, vol. 259, pp. 1127-1129.

35. J. Wong, E.M. Larson, J.B. Holt, P.A. Waide, B. Rupp, and R. Frahm: *Science*, 1990, vol. 249, pp. 1406-1409.

36. E.M. Larson, P.A. Waide, and J. Wong: *Rev. Sci. Instrum.*, 1991, vol. 61, pp. 53-57.

37. R. Frahm, J. Wong, J.B. Holt, E.M. Larson, B. Rupp, and P.A. Waide: *Physical Review B*, 1992, vol. 46, pp. 9205-9208.

38. I.O. Khomenko, V.I. Ponomarev, and I.P. Boronnskaya: *International Journal of Self-Propagating High-Temperature Synthesis*, 1994, vol. 3, pp. 117-122.

39. B.M. Volpe, V.V. Evsigneev, I.V. Milyukova, A.B. Mukhachyov, and D.A. Garkol: *International Journal of Self-Propagating High-Temperature Synthesis*, 1994, vol. 3, pp. 123-130.

40. Y.-M. Chiang, R.P. Messner, C.D. Terwilliger, and D.R. Behrendt: *Mater. Sci. Eng.*, 1991, vol. A144, pp. 63-74.

41. W.G. Fahrenholtz, K.G. Ewsuk, R.E. Loehman, and A.P. Tomsia: in *In Situ Reactions for Synthesis of Composites, Ceramics, and Intermetallics*, E.V. Barrera, S.G. Fishman, F.D.S. Marquis, N.N. Thadhani, W.E. Frazier, and Z.A. Munir, ed., TMS, Materials Park, OH, 1995, pp. 99-109.

42. R.E. Loehman, K. Ewsuk, and A.P. Tomsia: *J. Am. Ceram. Soc.*, 1996, vol. 79, pp. 27-32.

43. A. Mortensen and I. Jin: *Inter. Mater. Rev.*, 1992, vol. 37, pp. 101-128.

44. A. Mortensen, V.J. Michaud, and M.C. Flemings: *Journal of Metals*, 1993, vol. 45, pp. 36-43.

45. N.R. Morrow: *Industrial and Engineering Chemistry*, 1970, vol. 62, pp. 32-56.

46. W.G. Anderson: *J. Petroleum Technology*, 1987, vol. 39, pp. 1453-1468.

47. H. Fukunaga, X. Wang, and Y. Aramaki: *J. Mater. Sci. Letters*, 1990, vol. 9, pp. 23-25.

48. R.P. Messner and Y.-M. Chiang: *J. Am. Ceram. Soc.*, 1990, vol. 73, pp. 1193-1200.

49. H. Chen, M. Kaya, and R.W. Smith: *Mater. Letters*, 1992, vol. 13, pp. 180-183.

50. K. Suganuma: *Mater. Letters*, 1993, vol. 16, pp. 22-25.

51. H. Fukunaga and I. Tsuchitori: in *The Tenth International Conference on Composite Materials*, Proc. Conf., Whistler, Bristish Columbia, Canada, 1995, A. Poursartip and K. Street, ed., Woodhead Publishing Ltd., pp. 69-76.

52. I. Horsfall and M. Downing: in *In-Situ Composites: Science and Technology*, M. Singh and D. Lewis, ed., TMS, Materials Park, OH, 1994, pp. 149-157.

53. F. Delannay, C. Colin, Y. Marchal, L. Tao, F. Boland, P. Cobzaru, B. Lips, and M.-A. Dellis: *Journal de Physique IV*, 1993, vol. 3, pp. 1675-1684.

54. C. Colin, Y. Marchal, F. Boland, and F. Delannay: *Journal de Physique IV*, 1993, vol. 3, pp. 1749-1752.

55. A.-V. Ruzette, F. Boland, C. Colin, J.-M. Gilot, and F. Delannay: *New Eng. Mater.*, 1996, vol. 116-117, pp. 229-240.

56. Y. Chen and D.D.L. Chung: *J. Mater. Sci.*, 1996, vol. 31, pp. 2117-2122.

57. D.C. Dunand, J.L. Sommer, and A. Mortensen: in *Proc. 1992 Annual ASM/TMS Fall Meeting, Symposium on Processing and Fabrication of Advanced Materials for High Temperature Applications*, Proc. Conf., Chicago, Ill., 1992, T.S. Srivatsan and R.A. Ravi, ed., pp. 635-646.

58. D.C. Dunand, J.L. Somner, and A. Mortensen: *Metall. Trans. A*, 1993, vol. 24A, pp. 2161-2170.

59. D.B. Miracle: *Acta. metall. mater.*, 1993, vol. 41, pp. 649-684.

60. O. Kubaschewski, C.B. Alcock, and P.J. Spencer: *Materials Thermochemistry*, 6th ed., Pergamon Press, New York, 1993.

61. P.D. Desai: *J. Phys. Chem. Ref. Data*, 1987, vol. 16, pp. 109-124.

62. *Handbook of Chemistry and Physics*, 73rd ed., D.R. Lide, ed., CRC Press, London, 1992.

63. S. Shankar and L.L. Seigle: *Metall. Trans. A*, 1978, vol. 9A, pp. 1467-1476.

64. F.M. d'Heurle and R. Ghez: *Thin Solid Films*, 1992, vol. 215, pp. 19-25.

65. A. Mortensen, L.J. Masur, J.A. Cornie, and M.C. Flemings: *Metall. Trans. A*, 1989, vol. 20A, pp. 2535-2547.

66. J. Chadam, D. Hoff, E. Merino, P. Ortoleva, and A. Sen: *IMA J. Appl. Mathematics*, 1986, vol. 36, pp. 207-221.

67. J. Chadam and P. Ortoleva: in *Dynamics of Nonlinear Systems*, V. Hlavacek, ed., Gordon and Breach Science Publishers, New York, 1986, pp. 247-278.

68. J. Chadam, P. Ortoleva, and A. Sen: *SIAM J. Appl. Mathematics*, 1988, vol. 48, pp. 1362-1378.

69. R.B. Calhoun and A. Mortensen: *Metall. Trans. A*, 1992, vol. 23A, pp. 2291-2299.

70. *Smithells Metals Reference Book*, 6th ed., E.A. Brandes, ed., Butterworths, Boston, 1983.

71. A.K. Roy and R.P. Chhabra: *Metall. Trans. A*, 1988, vol. 19A, pp. 273-279.

72. A.P. Aldushin, T.M. Martemyanova, A.G. Merzhanov, B.I. Khaikin, and K.G. Shkadinskii: *Combustion, Explosives and Shock Waves*, 1972, vol. 8, pp. 159-167.

73. D. Chandley: in *U.S.-Japan Cooperative Science Program Seminar on "Solidification Processing for the 21st Century"*, Proc. Conf., Lenox, MA, 1994, National Science Foundation, U.S.A. and Japan Society for Promotion of Science, pp. 165-176.

74. V.K. Sikka, S.C. Deevi, and J.D. Vought: *Advanced Materials and Processes*, 1995, vol. 147, pp. 29-31.

75. J.-C. Bihr:*Le matériau composite NiAl - Al2O3*, Ph.D. thesis,1996, L'Université de Bordeaux.

76. T.A. Venkatesh and D.C. Dunand: *unpublished results* , 1996.